Article

SARS-CoV-2 infection triggers pro-atherogenic inflammatory responses in human coronary vessels

Natalia Eberhardt [1], Maria Gabriela Noval[2], Ravneet Kaur [1], Letizia Amadori [1], Michael Gildea[1], Swathy Sajja[1], Dayasagar Das[1], Burak Cilhoroz[1], O' Jay Stewart [3], Dawn M. Fernandez[4], Roza Shamailova[1], Andrea Vasquez Guillen [1], Sonia Jangra[5,6], Michael Schotsaert [5,6], Jonathan D. Newman[1], Peter Faries[7], Thomas Maldonado[8], Caron Rockman[8], Amy Rapkiewicz[9], Kenneth A. Stapleford[2], Navneet Narula[10], Kathryn J. Moore [1] & Chiara Giannarelli [1,3,10] ✉

Patients with coronavirus disease 2019 (COVID-19) present increased risk for ischemic cardiovascular complications up to 1 year after infection. Although the systemic inflammatory response to severe acute respiratory syndrome coronavirus 2 (SARS-CoV-2) infection likely contributes to this increased cardiovascular risk, whether SARS-CoV-2 directly infects the coronary vasculature and attendant atherosclerotic plaques remains unknown. Here we report that SARS-CoV-2 viral RNA is detectable and replicates in coronary lesions taken at autopsy from severe COVID-19 cases. SARS-CoV-2 targeted plaque macrophages and exhibited a stronger tropism for arterial lesions than adjacent perivascular fat, correlating with macrophage infiltration levels. SARS-CoV-2 entry was increased in cholesterol-loaded primary macrophages and dependent, in part, on neuropilin-1. SARS-CoV-2 induced a robust inflammatory response in cultured macrophages and human atherosclerotic vascular explants with secretion of cytokines known to trigger cardiovascular events. Our data establish that SARS-CoV-2 infects coronary vessels, inducing plaque inflammation that could trigger acute cardiovascular complications and increase the long-term cardiovascular risk.

Coronavirus disease 2019 (COVID-19), caused by severe acute respiratory syndrome coronavirus 2 (SARS-CoV-2), is uniquely marked by extraordinary tissue tropism and an array of clinical presentations, from asymptomatic infection to acute respiratory distress, multi-organ failure and death[1]. Ischemic cardiovascular events, such as acute myocardial infarction (AMI) and stroke, due to the underlying disruption of a chronically inflamed atherosclerotic plaque[2], are established clinical complications of COVID-19 (refs. 1,3). AMI and stroke can be triggered by several acute respiratory viral infections, including influenza virus[4]. However, patients with COVID-19 are >7-fold more likely to have a stroke

than patients with influenza[5], and their risk for both AMI and stroke remains high for up to 1 year after infection[6]. The extreme inflammatory response that occurs in severe cases of COVID-19, also known as cytokine storm[7], is likely a contributor to the increased risk for AMI and stroke. However, the possibility that SARS-CoV-2 directly affects the coronary vasculature, as documented for other distant organs (for example, kidney, gut, brain, adipose tissue and myocardium)[8], remains largely unexplored. In the lungs, tissue damage is aggravated by potent inflammasome activation in macrophages sensing SARS-CoV-2 virus[9]. A similar response in macrophages infiltrating arterial vessels affected

A full list of affiliations appears at the end of the paper. ✉e-mail: chiara.giannarelli@nyulangone.org

by the virus could boost plaque inflammation and risk for AMI and stroke in patients with COVID-19. Here we show, in coronary autopsy specimens from patients with COVID-19, that infiltrating macrophages were infected by SARS-CoV-2. Lipid-laden macrophages (foam cells), a hallmark of atherosclerosis at all stages of the disease[10], were more susceptible to SARS-CoV-2 infection than other macrophages, and this was dependent on the receptor neuropilin-1 (NRP-1). SARS-CoV-2 induced a strong pro-atherogenic inflammatory response in both macrophages and foam cells, which was largely recapitulated in an ex vivo SARS-CoV-2 infection of human vascular explants. This response may contribute to the ischemic cardiovascular complications in patients with COVID-19.

Spatial AI detects SARS-CoV-2 RNA in coronary macrophages

We analyzed coronary autopsy specimens (n = 27) from eight patients with RT–PCR-confirmed diagnosis of COVID-19 between May 2020 and May 2021. Demographics and clinical characteristics, including past medical history, cardiovascular risk factors and other relevant clinical information, were obtained from the patients' electronic medical records and autopsy reports (IRB i21-01587) (Fig. 1a and Supplementary Tables 1 and 2). The mean age was 69.6 years (median, 71; 59–84), and 75% of patients were male (6/8). Patients had coronary artery disease (8/8); three or more cardiovascular risk factors, such as hypertension (8/8), overweight or obesity (7/8), hyperlipidemia (7/8), type 2 diabetes (6/8) and chronic kidney disease (4/8); and some had a history of either myocardial infarction (1/8) or ischemic stroke (1/8) (Fig. 1a and Supplementary Table 1). Acute myocardial ischemia was diagnosed during hospitalization in three patients; one patient developed stroke; and four patients were found to have coronary stenosis (>50%) at autopsy. The patients, with the exception of one who was pronounced dead before admission, were hospitalized for an average of 17.6 d (range, 8–31) (Supplementary Table 2). One patient (Pt. 1) was hospitalized three times (for a total of 31 d) after the first diagnosis. Pt. 1 developed AMI and died during the third hospitalization, approximately 140 d after testing negative for COVID-19 (Fig. 1a and Supplementary Table 2). The clinical presentation, in-hospital course of the disease, COVID-19 treatments as well as macroscopic and microscopic autopsy pathology obtained from hospital medical records and autopsy reports are summarized in Supplementary Table 2.
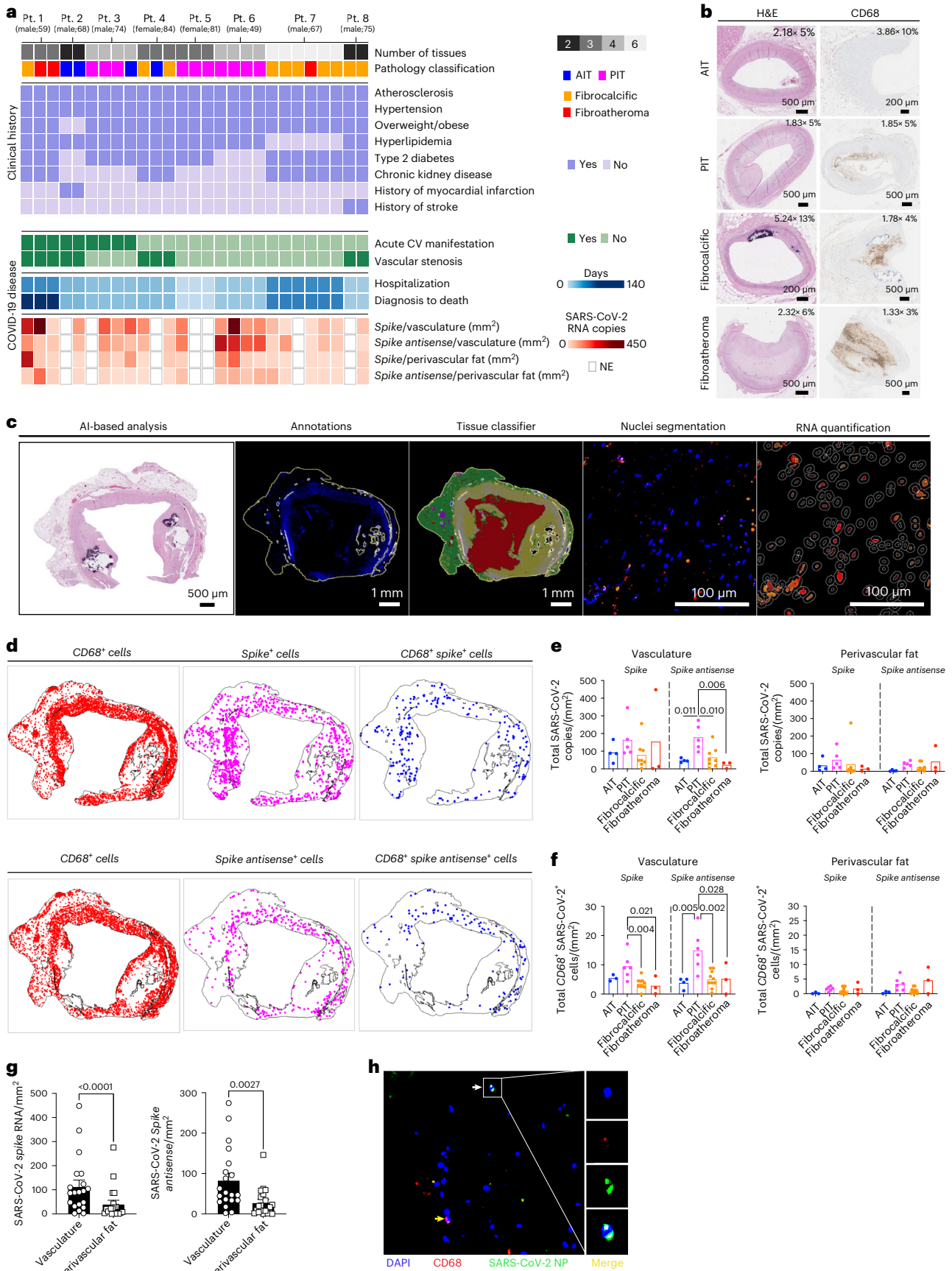
Sections of coronary arteries from all autopsies were stained with hematoxylin and eosin (H&E) and classified by a clinical cardiovascular pathologist (N.N.) as adaptive intimal thickening (AIT; n = 4), pathological intimal thickening with macrophage infiltration (PIT; n = 10), fibrocalcific plaque (n = 10) and fibroatheroma (n = 3) (Fig. 1a,b, Extended Data Fig. 1a, Supplementary Fig. 1 and Supplementary Table 3) according to established criteria[11,12]. Detailed pathological features, including presence of lipid pool, necrotic core and adventitial inflammation, were noted (Extended Data Fig. 1a). Immunohistochemical (IHC) staining for CD68+ cells showed that CD68+ cell count and frequencies were not significantly different among PIT, fibrocalcific lesions and fibroatheromas, whereas a larger positive stained area that corresponded to the necrotic cores was seen in fibroatheromas (Fig. 1b, Extended Data Fig. 1b,c and Supplementary Table 3).

To identify SARS-CoV-2 viral RNA (vRNA) in the autoptic coronary vasculature from patients with COVID-19, we performed RNA fluorescence in situ hybridization (RNA-FISH) analysis for the vRNA encoding the spike (S) protein. To establish whether SARS-CoV-2 infected the human coronary vasculature, we also probed the antisense strand of the S gene (S antisense), which is only produced during viral replication. A CD68 probe was used to identify macrophages infiltrating the coronary vessels in the same sections and establish the cellular localization of SARS-CoV-2 vRNA. Given the ability of SARS-CoV-2 to infect fat depots and accumulate vRNA in adipose tissue to trigger a strong pro-inflammatory response[13,14], we used a neural network artificial intelligence (AI) approach to classify the coronary arterial wall and

perivascular fat in each sample and nuclei segmentation to quantify the RNAscope probes in cells infiltrating the two tissues (Fig. 1c,d). In the coronary arterial wall, vRNA encoding the S protein and the antisense strand of the S gene were detected to different degrees in all the sections from all patients, indicating the presence of vRNA and replicative activity of the virus. SARS-CoV-2 S gene copy number was similar across AI, PIT, fibrocalcific and fibroatheroma coronary lesions (Fig. 1e). However, PIT coronaries showed a significantly higher copy number of the antisense strand of the S gene (S antisense), indicating higher viral replication in the vascular wall of these lesions (Fig. 1e). In particular, CD68+ cells expressing both the SARS-CoV-2 S and the antisense strand of S were significantly higher in the vasculature of PIT coronaries versus other pathologies (Fig. 1f). In perivascular fat, vRNA encoding the S protein was detected in 20 of the 21 sections, and the S antisense was detected in 19 of the 21 sections (Fig. 1a). Overall, each patient presented at least one section positive for S and S antisense vRNA (Fig. 1ae,f). Notably, the amount of S and S antisense strand vRNA was significantly lower in perivascular fat than in the corresponding arterial wall across all samples (Fig. 1g). The accumulation of viral protein material in the coronaries was confirmed by immunofluorescence (Fig. 1h).

PIT arterial lesions, which appeared more susceptible to SARS-CoV-2 infection, contained significantly more cells than other types of lesions and 4.8-fold more cells than corresponding perivascular tissue (2,691.8 ± 288.7 versus 697.6 ± 159.3 cells per mm²; P < 0.0001) (Extended Data Fig. 1d). The number of CD68 RNA+ cells in the coronary vasculature was significantly higher in both PIT and fibroatheromas than in other lesions (Extended Data Fig. 1e), which corresponded to a higher number of CD68 RNA+ cells in perivascular fat of PIT lesions than fibrocalcific lesions and similar to fibroatheromas (Extended Data Fig. 1e), suggesting a contributory role of direct infection of macrophages in the coronary susceptibility to SARS-CoV-2 infection. This possibility was further suggested by the significantly higher frequency of CD68+ cells expressing the S antisense strand of vRNA in PIT lesions and the corresponding perivascular fat (Extended Data Fig. 1f) as well as the significant association among SARS-CoV-2 vRNA copies with CD68 copy number in both arterial wall and perivascular fat (Extended Data Fig. 1g). The accumulation of SARS-CoV-2 vRNA encoding the S protein was higher in both the whole tissue and in the coronary wall from patients with COVID-19 with acute cardiovascular manifestations (Extended Data Fig. 1h).

To investigate the potential extension of SARS-CoV-2 infection to other cells, we focused on vascular smooth muscle cells (VSMCs), based on the spatial distribution of most SARS-CoV-2+ cells within the arterial wall of the coronaries, and we conducted additional RNAscope analyses that were guided by analyses of human and mouse single-cell RNA sequencing (scRNA-seq) datasets. An analysis, using scRNA-seq data from diseased human coronaries (Gene Expression Omnibus (GEO): GSE131780)[15], revealed that VSMCs express significantly higher levels of *ACTA2* compared to myeloid cells, whereas CD68 expression was specific to macrophages (Extended Data Fig. 2a). Additionally, we analyzed scRNA-seq data of lineage-tagged smooth-muscle-derived cells (VSMCs), isolated from the atherosclerotic aortic arches of ApoE$^{-/-}$ Tomato mice[16]. This analysis revealed that VSMCs in atherosclerotic lesions did not express significant levels of *Cd68* and maintained a high level of *Acta2* expression, although its expression was reduced compared to non-atherosclerotic conditions (Extended Data Fig. 2b). Based on these results, we used *ACTA2* probe to identify VSMCs and macrophages of VSMC origin as *ACTA2*+, and we included probes for the S and S antisense vRNA in the analysis to identify *ACTA2*+ infected cells. Notably, this analysis identified S+*ACTA2*+ cells and S antisense+*ACTA2*+ cells in human coronaries (Extended Data Fig. 2c); however, the median of the frequency of SARS-CoV-2-infected VSMCs (~0.14%) in human coronary was ~8 times lower than that of infected macrophages (~1.2%). These results show that, although SARS-CoV-2 can infect VSMCs, the number of infected VSMCs in human coronaries

a ... Number of tissues, Pathology classification (AIT, PIT, Fibrocalcific, Fibroatheroma), Clinical history (Atherosclerosis, Hypertension, Overweight/obese, Hyperlipidemia, Type 2 diabetes, Chronic kidney disease, History of myocardial infarction, History of stroke), COVID-19 disease (Acute CV manifestation, Vascular stenosis, Hospitalization, Diagnosis to death, Spike/vasculature (mm²), Spike antisense/vasculature (mm²), Spike/perivascular fat (mm²), Spike antisense/perivascular fat (mm²)).

b H&E and CD68 staining of AIT, PIT, Fibrocalcific, Fibroatheroma.

c AI-based analysis, Annotations, Tissue classifier, Nuclei segmentation, RNA quantification.

d CD68⁺ cells, Spike⁺ cells, CD68⁺ spike⁺ cells, CD68⁺ cells, Spike antisense⁺ cells, CD68⁺ spike antisense⁺ cells.

e Vasculature and Perivascular fat — Total SARS-CoV-2 copies/(mm²).

f Vasculature and Perivascular fat — Total CD68⁺ SARS-CoV-2⁺ cells/(mm²).

g SARS-CoV-2 spike RNA/mm², SARS-CoV-2 Spike antisense/mm².

h DAPI, CD68, SARS-CoV-2 NP, Merge.

was lower compared to the number of infected macrophages. To further investigate SARS-CoV-2 infection of VSMCs and lipid-laden VSMCs, which are associated with atherosclerosis[17–20], we infected primary human aortic VSMCs, as well as VSMCs loaded with cyclodextrin–cholesterol complexes (Extended Data Fig. 2d), with the SARS-CoV-2 USA WA1/2020 isolate. Approximately 18% of cultured VSMCs and

Fig. 1 | SARS-CoV-2 vRNA in human coronary arteries from deceased individuals with COVID-19 is identified using AI-based spatial analysis.
a, Categorical heat map of coronary autopsy specimens (*n* = 27) from deceased individuals with COVID-19 (*n* = 8) displays their sex, age and pathology classification into AIT, PIT, fibrocalcific plaques and fibroatheromas. The clinical history for each patient is shown. Summary of acute cardiovascular (CV) manifestations during COVID-19 disease progression, coronary stenosis (no: <50%; yes: >50%), hospitalization duration and time to death after COVID-19 diagnosis are also depicted. RNA copy numbers of S and S antisense vRNA normalized to vasculature and perivascular fat area (mm²) are shown. NE, not evaluated. **b**, Representative images of coronary samples stained with H&E and CD68 staining for each pathological classification. **c**, Representative images of in situ RNA-FISH AI-based analysis. After semi-automatic annotations, an AI-based neural network was used to classify the vasculature (yellow) and perivascular fat (green). Background and artifacts (red) were removed from the analysis. Next, nuclei segmentation classifier analysis and RNA quantification were performed using HALO AI and spatial analysis workflow. **d**, Representative images of spatial analysis showing the location of *CD68* RNA, SARS-CoV-2 S⁺ or S antisense⁺ cells and *CD68*⁺ SARS-CoV-2 RNA double-positive cells. **e**, Bar plots showing total SARS-CoV-2 vRNA copies of S and S antisense normalized by tissue area (mm²) in AIT (*n* = 4), PIT (*n* = 5), fibrocalcific (*n* = 8) and fibroatheroma (*n* = 3) coronary samples. **f**, Bar plots showing total *CD68*⁺ SARS-CoV-2 S⁺ or S antisense⁺ cells in the vasculature or perivascular fat regions normalized by tissue area (mm²) in AIT (*n* = 4), PIT (*n* = 5), fibrocalcific (*n* = 10) and fibroatheroma (*n* = 3) coronary samples. One-way analysis of variance (ANOVA) statistical analysis with post hoc Tukey's test for multiple comparisons was performed. **g**, SARS-CoV-2 S and S antisense quantification in vasculature and perivascular fat normalized by tissue area (mm²). Wilcoxon matched-pairs signed-rank test was performed (*n* = 20 per group). **h**, Representative images of of SARS-CoV-2 NP, CD68 and merge in human coronary. White arrow indicates CD68⁺ SARS-CoV-2 NP⁺ cell, and yellow arrow indicates CD68⁺ cell. Pt., patient.

13% of cholesterol-loaded VSMCs were S⁺, and the frequency of S antisense⁺*ACTA2*⁺ cells, indicating viral replication, was ~2.6% (Extended Data Fig. 2d,e). Taken together with our in vitro findings, which indicate that more than 79% of macrophages and over 90% of foam cells are S+, along with the discovery that more than 40% of both cell types are S antisense+, these results show that, although SARS-CoV-2 can infect VSMCs, macrophages are infected at a higher rate.

SARS-CoV-2 infection of human macrophages and foam cells

The accumulation of cholesterol-laden macrophages (foam cells) is a hallmark of atherosclerosis at all stages of the disease, from early PIT to late fibroatheroma lesions[10,12]. To investigate SARS-CoV-2 infection of both macrophages and foam cells, we differentiated human monocytes derived from human peripheral blood mononuclear cells into macrophages and treated them with oxidized low-density lipoprotein (oxLDL) complexed with Dil dye (Dil-Ox-LDL) to differentiate them into foam cells. To experimentally confirm our observation that SARS-CoV-2 can infect human plaque macrophages, macrophages and foam cells were infected either with icSARS-CoV-2 mNeonGreen (mNG) reporter virus, a modified virus that allows the use of mNG fluorescence as a surrogate readout for viral replication[21], or with SARS-CoV-2 USA WA1/2020 isolate. mNG expression confirmed the ability of SARS-CoV-2 to replicate in both cell types, although replication was higher in foam cells (Fig. 2a and Extended Data Fig. 3a). The significantly higher accumulation of nucleoprotein (NP) in foam cells compared to macrophages infected with SARS-CoV-2 USA WA1/2020 isolate (Fig. 2b and Extended Data Fig. 3b) confirmed a higher susceptibility of foam cells to the virus. In fact, although the frequency of NP⁺ foam cells fell between 24 hours post-infection (hpi) and 48 hpi, the proportion of SARS-CoV-2 NP⁺ foam cells remained significantly higher than that of NP⁺ macrophages

(Fig. 2b). Foam cells also accumulated more SARS-CoV-2 S vRNA than macrophages (Fig. 2c). SARS-CoV-2 vRNA genome was detectable in both macrophages and foam cells as early as 2 hpi, remained high up to 24 hpi but was reduced at 48 hpi in both cell types (Fig. 2d and Extended Data Fig. 3d). Notably, the expression of SARS-CoV-2 genes declined significantly faster in macrophages than foam cells, with significantly lower vRNA at 48 hpi (Fig. 2e). This dynamic temporal decay in vRNA levels indicates that macrophages are able to clear the virus faster than foam cells. Regardless, albeit being susceptible, both macrophages and foam cells did not sustain a productive formation of infectious viral particles as demonstrated by the results of the plaque assay using modified Vero E6 cells expressing the transmembrane protease serine 2 and human angiotensin-converting enzyme 2 (Vero E6-TMPRSS2-T2A-ACE2). These assays showed a progressive decline of viral titer conditioned media from infected macrophages and foam cells (Fig. 2f and Extended Data Fig. 3c). These results are consistent with abortive infection, a common outcome of many viral infections, with infected cells not producing replication-competent virus despite the production of vRNA[22–26].

SARS-CoV-2 triggers pro-atherogenic inflammatory responses

Based on the observation that SARS-CoV-2 replication was abortive in macrophages and foam cells and the evidence that the overreactive inflammatory response to SARS-CoV-2 is orchestrated by macrophages in other tissues[9,14,27], we investigated the immune response of macrophages and foam cells to SARS-CoV-2. Differential gene expression analysis of RNA-seq data from infected macrophages and foam cells identified shared and unique transcriptional signatures (Fig. 2g). As expected, the 1,254 shared genes included the SARS-CoV-2 viral genes. Other commonly upregulated genes were involved with antiviral

Fig. 2 | Differential IFN response and virus clearance dynamics in human macrophages and foam cells after SARS-CoV-2 in vitro infection.
a, Quantification of mNG reporter-positive macrophages and foam cells (*n* = 21 images per condition). **b**, Quantification of SARS-CoV-2-infected macrophages (24 hpi, *n* = 20; 48 hpi, *n* = 24) and foam cells (24 hpi, *n* = 20; 48 hpi, *n* = 18). Representative images for **a** and **b** show results at 48 hpi. Scale bars, 20 μm. One-way ANOVA with post hoc Tukey's test was performed. Data are presented as mean values ± s.e.m. **c**, RNA-FISH quantification of SARS-CoV-2 vRNA⁺ cell copies and frequency in macrophages (*n* = 37) and foam cells (*n* = 26). Data are presented as mean values ± s.e.m. Scale bars, 20 μm. Mann–Whitney *U*-test was performed. **d**, Heat map of SARS-CoV-2 viral genes reads in macrophages and foam cells. **e**, Heat map of log₂FC of SARS-CoV-2 viral genes in macrophages versus foam cells. The Wald test from the DESeq2 package was used to test for significance. Adjusted *P* values < 0.05 (FDR = 1%) were considered significant. **f**, Viral titer quantification of SARS-CoV-2-infected macrophages and foam cell culture supernatants (*n* = 6). Data are presented as mean values ± s.e.m. One-way ANOVA followed by Tukey's post hoc test was performed. **g**, Venn diagram of DEGs in infected versus non-infected macrophages, foam cells and shared genes. The Wald test from the DESeq2 package was used to test for significance. Bar plots show upregulated signaling pathways ranked by their combined score. *P < 0.05; **P < 0.01; ***P < 0.001. **h**, Heat maps of log₂FC of IFN response genes in macrophages and foam cells. The Wald test from the DESeq2 package was used to test for significance. Adjusted *P* values < 0.05 (FDR = 10%) were considered significant. Asterisk in parenthesis indicates the comparison of interaction between infection and timepoint terms of the model. *P < 0.05; **P < 0.01; ***P < 0.001. **i**, Heat map of log₂FC of SARS-CoV-2-infected macrophages versus foam (*n* = 3 biological replicates). The Wald test from the DESeq2 package was used to test for significance. Adjusted *P* values < 0.05 (FDR = 10%) were considered significant. **j**, Longitudinal kinetic plots of combined IFN response and SARS-CoV-2 genes scores. Data are presented as median and 25th–75th quartile log₂FCs of SARS-CoV-2-infected versus non-infected cells. Hypothesis testing was performed using the Wilcoxon rank-sum test.

responses and SARS-CoV-2 infection, including interferon (IFN) signaling pathways and antiviral processes by type I and II IFN signaling, oligoadenylate synthetase (OAS) antiviral response, negative regulation of viral replication and viral lifecycle as well as complement activation and cytokine signaling. ISG15 antiviral signaling, which dampens IFN signaling and has been implicated in the hyperinflammatory response
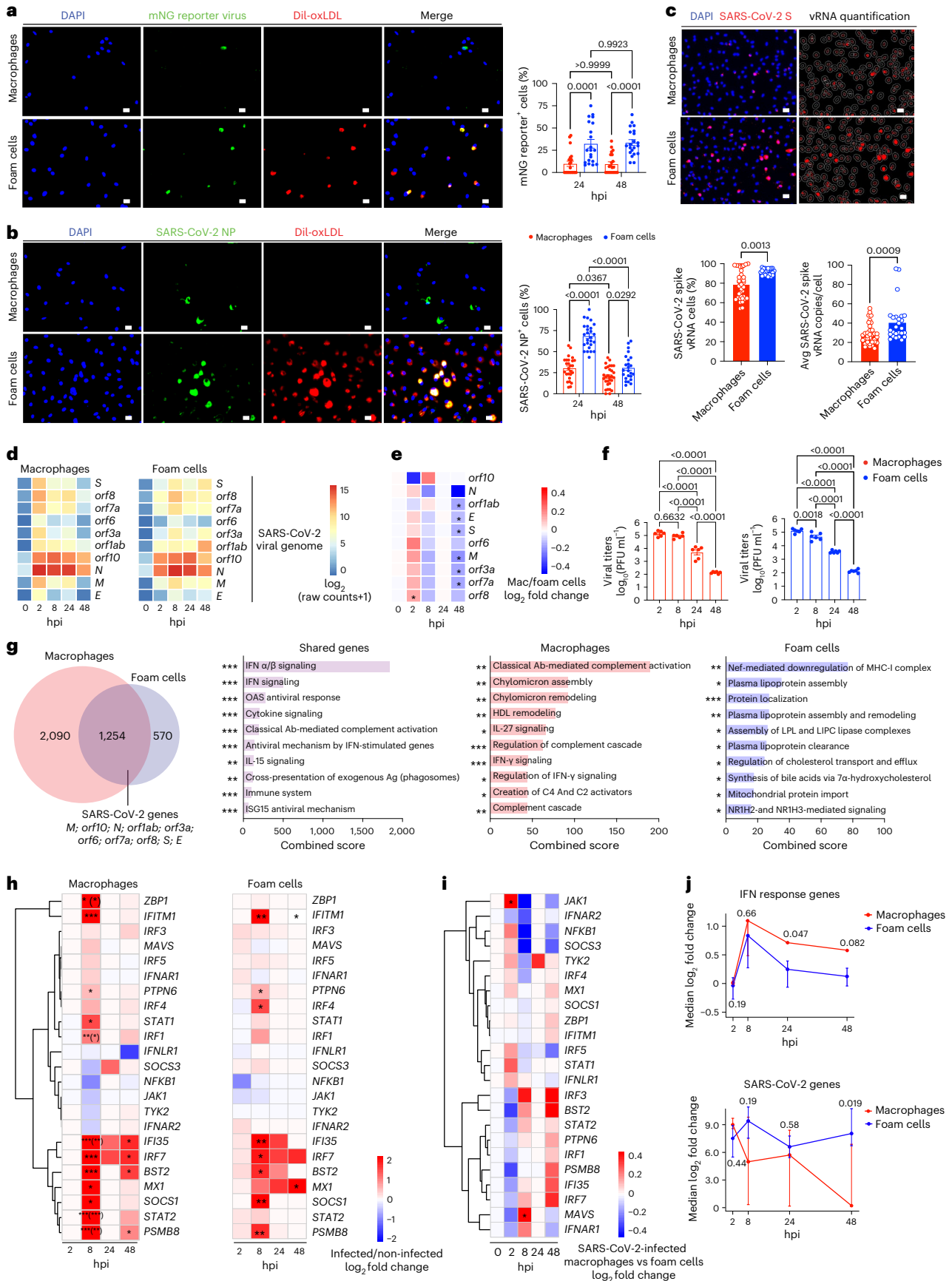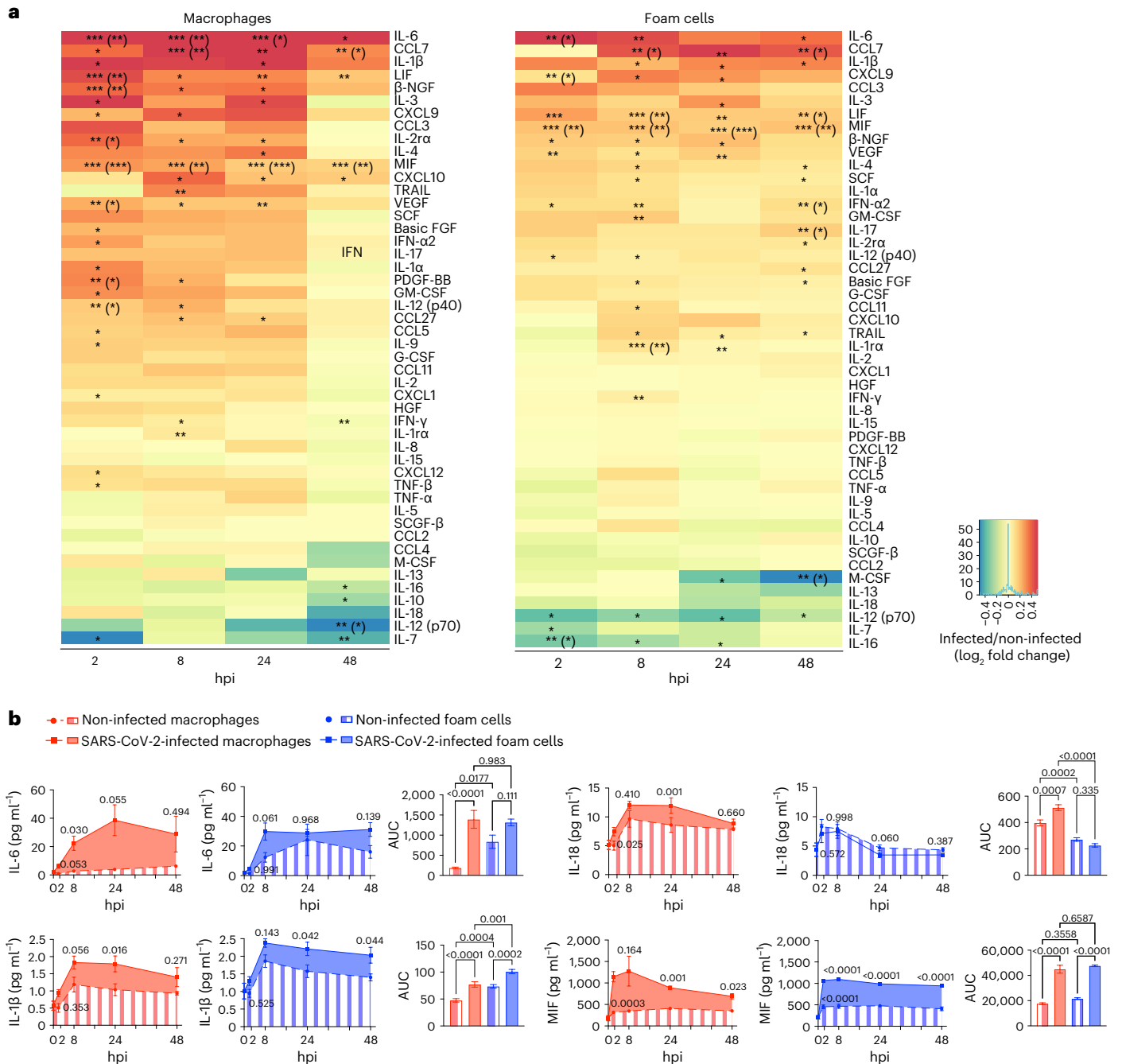
Fig. 3 | Analysis of cytokine release dynamics after SARS-CoV-2 infection.
a, Heat map of cytokines and chemokines secreted from SARS-CoV-2-infected macrophages and foam cells. Data are shown as log$_2$FC of infected versus uninfected cells. P values were calculated by two-tailed unpaired t-test, *P < 0.05; **P < 0.01; ***P < 0.001. Adjusted P values (Benjamini–Hochberg method) are presented in parentheses. **b**, Kinetic plots show the AUC of cytokines secreted by SARS-CoV-2-infected macrophages and foam cells versus non-infected cells (n = 4 biological replicates, technical duplicates). For AUC comparisons, one-way ANOVA after Tukey's multiple comparisons test was performed. Kinetics differences were evaluated by two-way ANOVA followed by Sidak's multiple comparisons test. Data are presented as mean ± s.e.m. Bar plots show the quantification of the AUC for each cytokine. One-way ANOVA statistical analysis after Tukey's multiple comparisons test was performed.

associated with COVID-19 severity[27,28], was also upregulated in both cell types (Fig. 2g and Extended Data Fig. 3e). Infected macrophages expressed a unique transcriptional signature associated with classical complement cascade activation, complement cascade (Fig. 2g and Extended Data Fig. 3f) as well as IFN-γ signaling and its regulation and IL-27 signaling, which induces IFN/STAT1-dependent genes[29] and regulation of cytokine pathways (Fig. 2g). We also observed a significant upregulation of certain lysosomal genes in infected macrophages compared to foam cells at 2 hpi and 8 hpi (Extended Data Fig. 3g,h),

revealing a more robust lysosomal response in macrophages that can contribute to the more efficient viral clearance observed in macrophages. Our analysis showed a significant increase in genes encoding proteins involved in lipid uptake in infected macrophages versus foam cells (Fig. 2g and Extended Data Fig. 3i). These included *CD36*, encoding for the CD36 receptor for oxLDL, as well as *LDLR*, encoding LDL receptor, which is the primary cholesterol-carrying lipoprotein in plasma and facilitates the uptake of LDL into cells through endocytosis. In contrast, genes encoding proteins associated with lipid

efflux (that is, *ABCG1* and *ABCA1*) were significantly downregulated in infected macrophages compared to foam cells (Extended Data Fig. 3i). Lipids and lipid droplets play crucial roles in viral lifecycle, including SARS-CoV-2 (refs. 30–32). By promoting lipid uptake and accumulation in macrophages, SARS-CoV-2 may create a cellular environment that is favorable for viral infection.

The unique infected foam cell transcriptional signature included 570 genes (Fig. 2g and Extended Data Fig. 2e). The top upregulated signaling pathways involved the downregulation of major histocompatibility complex class I (MHC-I), a response induced by many viruses to evade immune recognition[33,34]. Infected foam cells also upregulated processes and signaling pathways involved in the regulation of lipid metabolism that may facilitate viral entry and replication[32].

The activation of a type I IFN response in both SARS-CoV-2-infected macrophages and foam cells was consistent with the upregulation of several genes, with the strongest response observed at 8 hpi (Fig. 2h and Extended Data Fig. 3e). In macrophages, significantly upregulated genes included *IRF1*, a transcriptional activator of IFN-α and IFN-β, as well as genes induced by IFN-α, IFN-β and IFN-γ; *MX1*, encoding a GTP-binding protein Mx1 that has antiviral activity against RNA viruses, including SARS-CoV-2 (refs. 35,36); as well as *STAT1* and *STAT2*. *IRF7*, known to induce type I IFN responses, and the viral restriction factor *IFITM1* (ref. 37), were also upregulated in SARS-CoV-2-infected macrophages (Fig. 2h). The IFN response in SARS-CoV-2-infected foam cells was similar, although there was a delayed upregulation of *MX1* that occurred only at 48 hpi, consistent with the higher vRNA and protein accumulation seen in foam cells, and only foam cells upregulated *IRF4*, which inhibits MyD88 signaling and is expressed in M2-like macrophages[38]. Moreover, the expression of *STAT1* and *STAT2* were not significantly increased (Fig. 2h), suggesting a distinct IFN-induced JAK/STAT signaling regulation in infected macrophages. A direct comparison between infected macrophages and infected foam cells confirmed a stronger IFN response in macrophages compared to foam cells with a significant upregulation of *JAK1* at 2 hpi and of *MAVS*, encoding mitochondrial antiviral signaling protein that is essential for antiviral innate immunity[39–41], at 8 hpi (Fig. 2i).
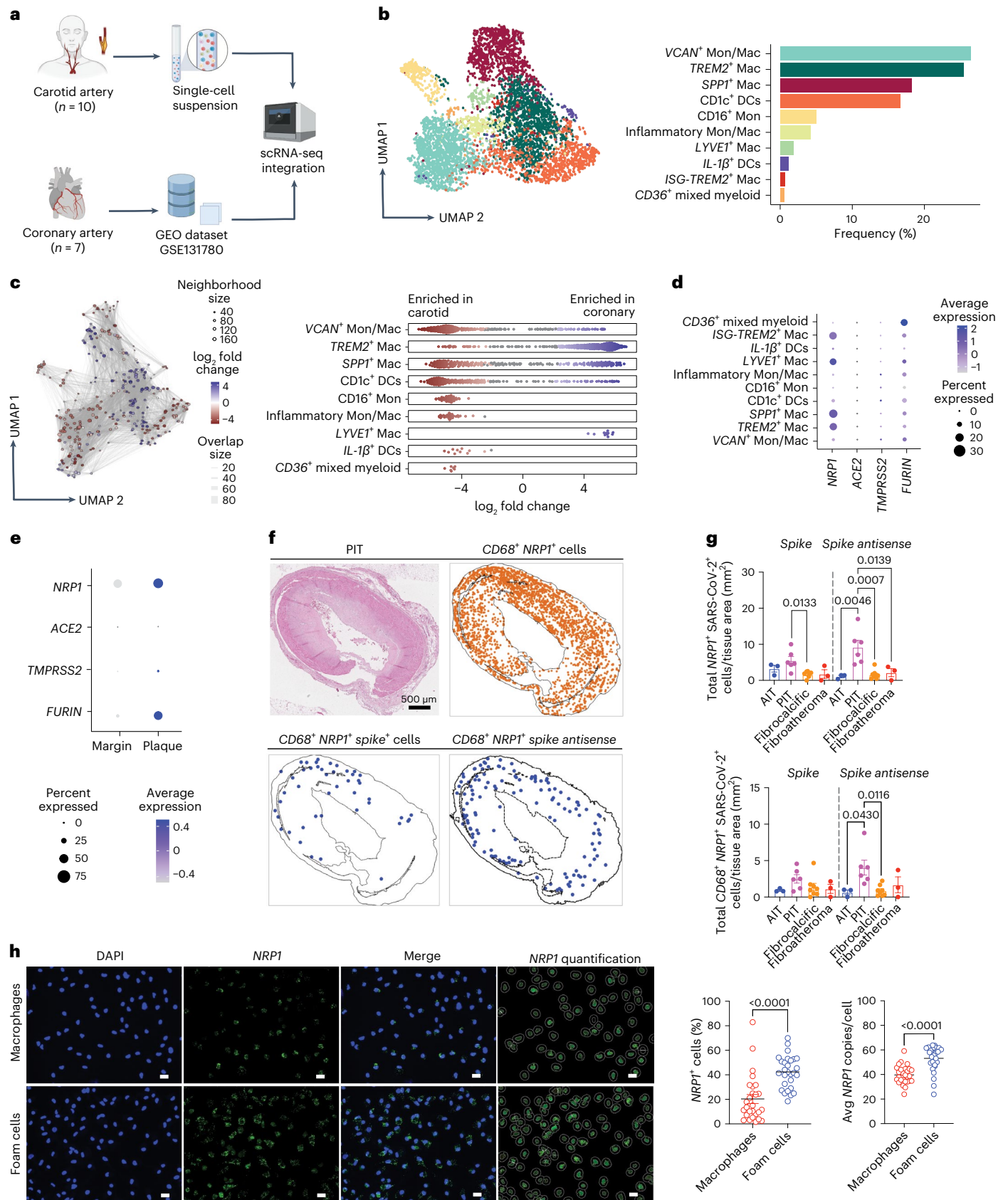
The analysis of the dynamic changes in the IFN-I response between macrophages and foam cells using an IFN and SARS-CoV-2 gene signature scoring method (Methods) revealed important kinetic differences in the IFN response and SARS-CoV-2 gene expression between macrophages and foam cells (Fig. 2j). Although from 2 hpi to 24 hpi there was no significant difference in the SARS-CoV-2 genome score between infected macrophages and foam cells, at 48 hpi a significant reduction in the SARS-CoV-2 genome score was observed in macrophages but not in foam cells, indicative of differential vRNA stability. In parallel, the IFN-I score increased in both infected macrophages and foam cells, but foam cells displayed a significant decline in the IFN-I score at 24 hpi and 48 hpi. Given the well-established knowledge that type I IFN reduces SARS-CoV-2 infection and replication, thereby promoting viral clearance[42–45], the robust and sustained type I IFN response in macrophages likely contributes to decreased viral persistence. In addition, macrophages and foam cells did not show differences in apoptotic pathway activation, such as Caspase-8 secretion (Extended Data Fig. 3j). Several pro-inflammatory and pro-atherogenic cytokine and chemokine genes were significantly upregulated in both infected macrophages and foam cells (Extended Data Fig. 4a,b). These included *CCL7*, *TNFSF10* (also known as *TRAIL*), *CXCL10* and *CCL3*. Infected macrophages uniquely upregulated *CXCL9*, *CXCL12* and *CLEC11A*, whereas foam cells upregulated *TNFA*, *CCL5* and *CCL2*.

To further investigate the inflammatory profile of macrophages and foam cells in response to SARS-CoV-2 infection, we quantified the secretion of cytokines and chemokines for up to 48 hpi (Fig. 3 and Extended Data Fig. 4b). Several pro-inflammatory and pro-atherogenic cytokines (for example, IL-6, CCL7, IL-1β, β-NGF, IL-3, LIF, MIF, CXCL9, IFN-α and IFN-γ) were released by both infected macrophages and foam cells (Fig. 3a). Among these are key cytokines known to trigger ischemic cardiovascular events, including IL-6, a candidate therapeutic target in ongoing clinical trials[46], and IL-1β, whose inhibition reduced secondary cardiovascular events in high-risk post-myocardial infarction patients[47] (Fig. 3b). Moreover, the release of macrophage migration inhibitory factor (MIF), a pro-atherogenic and inflammatory cytokine that has been implicated in intima-media thickening, lipid deposition and plaque instability[48], was increased in both cell types after infection. This analysis also revealed differential expression patterns of secreted cytokines by macrophages and foam cells in response to SARS-CoV-2 infection, suggesting distinct inflammatory responses between macrophages and foam cells. For example, the pro-atherogenic cytokine IL-18 (ref. 49) was significantly released by infected macrophages but not foam cells, whereas IFN-α2, a type I IFN response cytokine that inhibits viral replication[50], was significantly released by infected foam cells but not macrophages (Extended Data Fig. 4b). Notably, we detected significant differences in release of many of these cytokines over time between uninfected macrophage and foam cells, suggesting that differences in the baseline inflammatory status of each cell type influence their responses to the virus (Fig. 3b and Extended Data Fig. 4b).

SARS-CoV-2 boosts inflammation of atherosclerotic vascular explants

To determine whether the macrophage and foam cell pro-inflammatory response to SARS-CoV-2 that we observed in vitro also occurs in human vascular tissue, we infected human atherosclerotic vascular explants with SARS-CoV-2 USA WA1//2020 isolate (Fig. 4a). SARS-CoV-2 vRNA encoding the structural proteins spike (S), envelope (E), membrane (M) and nucleocapsid (N), as well as open reading frames (ORFs) encoding non-structural accessory proteins, were detectable in infected plaques as early as 24 hpi and for up to 72 hpi (Fig. 4b). S and N protein expression and virus-like particles were observed in infected atherosclerotic plaques (Extended Data Fig. 5a,b). However, viral titer decreased over time with no infectious virus isolated from the conditioned media of either infected cells or tissues using a plaque assay up to 72 hpi, suggesting abortive replication in the vascular explants (Fig. 4c). Regardless, SARS-CoV-2 infection induced a strong type I IFN transcriptional response in infected plaques reflected by the early upregulation of transcription factors and genes involved in response to viral infections, such as *IRF7*, *JAK1* and *IFITM1* at 2 hpi; *IFNAR*, *IRF4*, *IRF1*, *MX1*, *PTPN6*, *IFNA1*, *STAT1* and *STAT2* at 24 hpi; *IRF1*, *IFNA7* and *IFI35* at 48 hpi; and *IFNA16* at 72 hpi. Genes involved in the negative regulation of IFN signaling (that is, *SOCS1* and *SOCS3*) were also upregulated, likely reflecting the activation of regulatory signaling (Fig. 4d). Interestingly, SARS-CoV-2 infection triggered the expression of viral receptors and entry factors, such as *ACE2*, *NRP1*, *FURIN*, *TMPRSS4*, *TMPRSS11A* and *CTSB* at 24 hpi, suggesting that the virus facilitates its own entry in host cells (Fig. 4e). SARS-CoV-2 also initiated a transcriptional pro-inflammatory response that largely recapitulated that seen in cultured macrophages and foam cells. This included the upregulation of pro-atherogenic cytokines, such as *IL1B*, *IL6*, *MIF*, *ILB*, *TNF*, *IL7* and *CCL5*, as well as chemokines, such as *CCL2*, *CCL3*, *CCL4*, *CCL5*, *CXCL9*, *CCL27*, *CCL7*, *CCL6*, *CXCL1*, *CXCL8*, *CXCL9* and *CXCL12*. Anti-inflammatory cytokines, such as *IL10* and *IL13*, were downregulated, further supporting a strong pro-atherogenic inflammatory response to SARS-CoV-2 infection in human atherosclerotic plaques (Fig. 4f and Extended Data Fig. 5c). Analysis of the secretome of infected plaques revealed similar pro-inflammatory protein changes (Fig. 4g). SARS-CoV-2-infected plaques released several pro-atherogenic cytokines and chemokines, including IL-6, IL-1β and IFN-α2, as well as CCL2, CCL3, CCL4 and CCL7 (Fig. 4g). The release of cytokines and chemokines was substantially higher at 72 hpi. However, only IL-6, IL-1β, IFN-α2 and CCL3 were secreted at significantly higher amounts over time calculated as area under the curve (AUC) (Fig. 4h and Extended Data Fig. 5d). A stronger inflammatory response was observed in SARS-CoV-2-infected atherosclerotic plaques versus

Fig. 4 | Host immune response to SARS-CoV-2 infection of human atherosclerosis vascular explants. a, Schematics of experimental approach of human carotid vascular explants infection with SARS-CoV-2. **b**, Heat map of SARS-CoV-2 viral reads in carotid vascular explants at baseline (0 hpi), 24 hpi, 48 hpi and 72 hpi. **c**, Infectious viral titer quantification of SARS-CoV-2-infected carotid plaque culture supernatants ($n = 3$ biological samples, technical duplicates). Data are presented as mean values ± s.e.m. One-way ANOVA followed by Tukey's post hoc test was performed. **d**, Heat map showing the standardized z-scored expression of IFN response genes in SARS-CoV-2-infected carotid vascular samples at different times after infection. **e**, Heat map of standardized z-scored expression of selected host viral receptors and entry factors in SARS-CoV-2-infected human carotid vascular samples. **f**, Heat map of standardized z-scored gene expression of cytokine and chemokine genes in SARS-CoV-2-infected human carotid vascular explants at different times after infection. **g**, Heat map of cytokines and chemokines secreted from SARS-CoV-2-infected human

atherosclerotic plaques. Data are shown as $\log_2$FC of infected versus non-infected samples. P values were calculated by two-tailed paired t-test, $*P < 0.05$; $**P < 0.01$; $***P < 0.001$. P values in parentheses were adjusted using the Benjamini–Hochberg method. **h**, Kinetic plots show the AUC of cytokines and chemokines secreted by non-infected or SARS-CoV-2-infected carotid plaques ($n = 3$ donors, technical duplicates). Data are presented as mean values ± s.e.m. Two-way ANOVA statistical analysis after Sidak's multiple comparisons test was performed. Paired t-test was performed to compare the AUC of two groups. **i**, Plot showing the relative expression of secreted cytokines and chemokines between SARS-CoV-2-infected atherosclerotic plaque versus vascular margins. Relative expression is represented in $\log_2$FC colored scale. Statistical significance is expressed as dot size. Statistically significant values are represented as circles, and non-significant changes are represented as diamonds. P values were calculated by two-tailed unpaired t-test. P values were adjusted using the Benjamini–Hochberg method.

non-atherosclerotic paired surgical margins, as shown by the significantly higher release of several cytokines (for example, IFN-γ, IFN-α2, IL-1β, IL-17, TNF-α, TNF-β, CCL3, CCL4 and CCL7) from infected plaques mainly at 48 hpi (Fig. 4i). These findings suggest that SARS-CoV-2 infection triggers a hyperactivated immune response mainly within atherosclerotic lesions, a response that could contribute to the increased risk of ischemic cardiovascular events in patients with COVID-19 with underlying atherosclerosis.

NRP1⁺ macrophages increase plaque susceptibility to SARS-CoV-2

To elucidate the vascular susceptibility to SARS-CoV-2 infection, we evaluated the expression of the main viral entry receptors and co-factors in the aorta, coronary and tibial arteries using gene expression data

publicly available from the Genotype-Tissue Expression (GTEx) project (https://gtexportal.org/home/). The lung, heart tissue and whole blood were also included in this analysis (Extended Data Fig. 6a,b). We specifically focused on *ACE2*, encoding the first reported receptor for SARS-CoV-2 entry into human cells; neuropilins (*NRP1* and *NRP2*); and the proteases *TMPRSS2*, *FURIN*, cathepsin B (*CTSB*) and cathepsin L (*CTSL*), required to cleave the S protein for viral entry and replication[51–54]. Bulk RNA sequencing (RNA-seq) analysis showed a similar expression pattern for *ACE2*, *NRP1*, *NRP2*, *FURIN* and *CTSB* and *CTSL* in the aorta, coronary and tibial arteries compared to the lung, with the exception of *TMPRSS2*, which was expressed at lower levels in the arteries (Extended Data Fig. 6b).

To investigate the cellular expression of SARS-CoV-2 receptor and entry factors in the human atherosclerotic tissue, we performed

an integrated scRNA-seq analysis of human carotid plaques from 10 patients undergoing carotid endarterectomy (CEA) and atherosclerotic coronary data obtained from seven coronary samples from four heart transplant cases publicly available in the GEO (GSE131780) (Fig. 5a)[15]. The two datasets were merged using the Harmony algorithm,

resulting in 16 subclusters of immune cells that corresponded to all major immune population infiltrating human atherosclerotic plaques (Extended Data Fig. 6c). The SARS-CoV-2 entry receptors and host entry factors such as *NRP1*, a SARS-CoV-2 receptor that can bind FURIN-cleaved S protein to facilitate SARS-CoV-2 viral entry,

Fig. 5 | Single-cell expression of SARS-CoV-2 receptor and entry factors in human atherosclerotic tissue. a, scRNA-seq of human carotid (*n* = 10) and coronary (GSE131780) (*n* = 7) tissue samples. **b**, UMAP visualization of myeloid cell subclusters from coronary (1,960 cells) and carotid (2,900 cells) samples. Bar plot shows the frequency of each myeloid cluster. **c**, Neighborhood graph of the results from MiloR differential abundance testing. Nodes represent neighborhoods, colored by their log₂FC between carotid (red) and coronary (blue) samples. Non-differential abundance neighborhoods are in white (FDR = 10%), and node size reflects the total number of cells in each neighborhood. Beeswarm plots show the log₂FC distribution of neighborhoods between tissue type (FDR = 10%). **d**, Dot plot of the SARS-CoV-2 viral entry factor average gene expression and percent of expression in each myeloid subcluster.

e, Dot plots showing the frequency of cells expressing SARS-CoV-2 viral entry factors colored by average expression in atherosclerotic plaque lesions and paired vasculature margins. **f**, Representative images of H&E and spatial analysis of PIT coronary sample showing the location of *CD68*⁺*NRP1*⁺ cells, *CD68*⁺*NRP1*⁺ SARS-CoV-2 S⁺ or S antisense⁺ cells. **g**, Bar plots showing total *NRP1*⁺ SARS-CoV-2 vRNA⁺ and *CD68*⁺*NRP1*⁺ SARS-CoV-2 vRNA⁺ cells normalized by tissue area (mm²) in AIT (*n* = 3), PIT (*n* = 6), fibrocalcific (*n* = 8) and fibroatheroma (*n* = 3) coronaries. **h**, Representative images and RNA-FISH quantification of frequency of *NRP1*⁺ cells and average *NRP1* copies per cell in non-infected macrophages (*n* = 27) and foam cells (*n* = 28). Scale bars, 20 µm. Statistical analysis was performed using unpaired two-tailed Student's *t*-test. Avg, average; Mac, macrophages; Mon, monocytes.

and the proteases *CTSB* and *CTSL* were highly expressed in myeloid subclusters, whereas *ACE2* and the transmembrane serine proteases *TMPRSS2, TMPRSS4, TMPRSS11A* and *TMPRSS11B* were either undetectable or expressed at low levels (Extended Data Fig. 6d). Based on this observation, we subclustered myeloid cells (Fig. 5b and Extended Data Fig. 6e) and identified two clusters of dendritic cells (DCs), three clusters of monocytes/macrophages, one cluster of mixed myeloid cells and four clusters of macrophages/foam cells that were annotated based on the expression of canonical markers (Extended Data Fig. 6f). To identify significant differences in the abundance of myeloid cells between carotid and coronary arteries, we performed Milo differential neighborhood abundance testing[55]. This analysis revealed that *TREM2*⁺ macrophages were enriched in coronary tissue, whereas *VCAN*⁺ monocytes/macrophages and CD1c⁺ DCs were enriched in carotid samples. *CD16*⁺ monocytes, inflammatory monocyte/macrophages, *IL1B*⁺ DCs and *CD36*⁺ mixed myeloid cells were exclusively present in carotid samples, whereas *LYVE1*⁺ macrophages were present in coronaries. *SPP1*⁺ macrophages were present in both tissues (Fig. 5c). Overall, *NRP1* was strongly expressed in *TREM2*⁺, *SPP1*⁺, *LYVE1*⁺ and IFN-stimulated gene (*ISG*)⁺*TREM2*+ macrophages, clusters that also expressed *FURIN*. *ACE2* and *TMPRSS2* were undetectable in the analyzed myeloid cells (Fig. 5d). *NRP1* and *FURIN* gene expression was higher in human atherosclerotic plaques compared to paired normal margins (Fig. 5e), suggesting a key role for NRP-1 in mediating SARS-CoV-2 infection of the atherosclerotic vasculature. Spatial RNA-FISH analysis of human coronary autopsy specimens from patients with COVID-19 confirmed that macrophages expressing *NRP1* (*CD68*⁺*NRP1*⁺ cells) infiltrated coronary lesions and that these cells also expressed SARS-CoV-2 S vRNA and the antisense strand of the S gene, indicating viral replication (Fig. 5f,g). A higher number of *NRP1*⁺ macrophages expressing the antisense strand of the S gene were found in PIT coronary lesions, consistent with the greater susceptibility of PIT lesions to infection (Fig. 5g).

Given that *NRP1* was highly expressed in *TREM2*⁺ macrophages, which are considered foamy plaque macrophages[56], and it was significantly higher in foam cells versus macrophages in vitro (Fig. 5h), we performed additional experiments using silencing RNA (siRNA)

to specifically inhibit NRP-1 expression and investigate its impact on SARS-CoV-2 infection (Fig. 6a,b and Extended Data Fig. 7a–f). We achieved efficient reduction (~80%) of *NRP1* gene expression in both macrophages and foam cells, which was confirmed by western blotting and RNAscope analysis (Extended Data Fig. 7a–d and Supplementary Fig. 2). Upon *NRP1* silencing of infected cells, we observed a significant decrease in the frequency of SARS-CoV-2 S antisense⁺ macrophages and foam cells as well as a reduced frequency of SARS-CoV-2 S⁺ foam cells (Fig. 6a and Extended Data Fig. 7e). These findings were confirmed using EG00229, a small molecule that prevents SARS-CoV-2 binding to the B1 domain of NRP-1 and reduces SARS-CoV-2 infection of cell lines[53,54] (Fig. 6b and Extended Data Fig. 7f).

We next asked whether *NRP1* silencing or blocking using EG00229, which reduced the infection of macrophages and foam cells in vitro, would reduce the inflammatory response to SARS-CoV-2. The results revealed that NRP1 silencing increased the baseline inflammatory state of uninfected macrophages and, to a lesser extent, of foam cells, as evidenced by the release of several cytokines and chemokines (Extended Data Fig. 8a). Notably, this inflammatory state persisted upon SARS-CoV-2 infection, with infected *NRP1*-silenced cells exhibiting higher levels of cytokines induced by the virus, such as IL-6 and MIF, compared to non-infected NRP1-silenced cells (Fig. 6c and Extended Data Fig. 8a). In foam cells, NRP-1 silencing had more modest effects on both uninfected and infected cells, with the release of inflammatory cytokines primarily driven by SARS-CoV-2 infection (Fig. 6 and Extended Data Fig. 8a). The results are consistent with the anti-inflammatory functions of NRP-1 in myeloid cells and increased inflammation when NRP1 expression is lost[57,58]. Interestingly, the use of EG00229 yielded similar inflammatory patterns, but some differences may suggest potential off-target effects associated with this inhibitor (Fig. 6d). To investigate the potential modulation of TGF-β by *NRP1* inhibition, we examined the secretion of TGF-β in infected macrophages and foam cells (Extended Data Fig. 8b). Although, in macrophages, TGF-β expression was unaffected by SARS-CoV-2 infection, and the inhibition of NRP-1 did not influence its expression, we observed an increase in TGF-β levels in infected foam cells due to

Fig. 6 | Abrogation of NRP-1-mediated SARS-CoV-2 infection. a, Representative images of AI-based RNA-FISH quantification showing *NRP1* RNA, SARS-CoV-2 S and S antisense⁺ cells. Scale bars, 50 µm. Quantification of the frequency of SARS-CoV-2 S⁺ and SARS-CoV-2 S antisense⁺ cells in macrophages and foam cells treated with non-targeting siRNA control or siRNA NRP1 at 24 hpi. Data are presented as mean values ± s.e.m. Statistical analysis was performed using unpaired two-tailed Student's *t*-test. **b**, Representative images of RNA-FISH quantification showing *NRP1* RNA, SARS-CoV-2 S and S antisense⁺ cells. Scale bars, 20 µm. Quantification of the frequency of SARS-CoV-2 S⁺ and SARS-CoV-2 S antisense⁺ cells in macrophages and foam cells with and without NRP1 inhibition (EG00229 trifluoroacetate) at 24 hpi. **c**, Heat map of differentially secreted cytokine and chemokine levels from SARS-CoV-2-infected macrophages and foam cells (*n* = 4–5) after treatment with siRNA control or siRNA NRP1 at 24 hpi. Adjusted *P* values < 0.05 were considered significant. Asterisk indicates an adjusted *P* value < 0.05 for the comparison of SARS-CoV-2 infected and treated

with NRP1 siRNA versus infected and siRNA control. Asterisks in parentheses indicate nominal *P* < 0.05 for the comparison between macrophages versus foam cells, *P < 0.05; **P < 0.01; ***P < 0.001. **d**, Heat map of differentially secreted cytokine and chemokine levels from SARS-CoV-2-infected macrophages and foam cells after NRP1 blocking (EG00229 trifluoroacetate). Results are shown as log₂FC between infected and non-treated conditions. Adjusted *P* values < 0.05 were considered significant. Asterisk indicates an adjusted *P* value < 0.05 for the comparison of SARS-CoV-2 infected and treated versus infected and vehicle-treated conditions. Asterisks in parentheses indicate nominal *P* value < 0.05 for the comparison between macrophages versus foam cells, *P < 0.05; **P < 0.01; ***P < 0.001. **e**, Plot showing the relative expression of secreted cytokines and chemokines from NRP1 blocking (EG00229 trifluoroacetate) treated versus untreated SARS-CoV-2-infected atherosclerotic plaques at 48 hpi. Relative expression is represented in log₂FC colored scale. Circles represent statistically significant results, and non-significant changes are represented as diamonds.

SARS-CoV-2 infection that was partially reduced by NRP-1 inhibition. NRP-1 blocking increased the release of secreted IL-6 and CCL2 from SARS-CoV-2-infected human atherosclerotic vascular explant tissue.

The release of IL-1β and IL-18 was also increased but not significantly (Fig. 6e). Taken together, these findings suggest that atherosclerotic plaques are particularly susceptible to SARS-CoV-2 infection, which

triggers a hyperactivated immune response that could contribute to the increased risk of ischemic cardiovascular events in patients with COVID-19 with underlying atherosclerosis. Although inhibiting the host entry factor NRP-1 expressed by macrophages infiltrating coronary lesions in humans reduced SARS-CoV-2 infection, it also induced a strong inflammatory response, indicating that alternative strategies will be necessary to prevent SARS-CoV-2 infection of coronary vessels and its downstream consequences.

Discussion

Although SARS-CoV-2 is considered a respiratory virus, patients with COVID-19 have been shown to be at increased risk of cardiovascular complications, including myocardial infarction and stroke. Our study provides evidence of SARS-CoV-2 presence in human coronary vasculature and demonstrates viral tropism for vascular lesion macrophages in individuals with severe COVID-19. We found evidence of SARS-CoV-2 replication in all analyzed human autopsy coronaries regardless of their pathological classification, although viral replication was highest in PIT coronary lesions—early-stage lesions that progress to more advanced atherosclerotic plaques[11,12]. It is well established that, as lesions progress to more advanced stages, such as fibroatheromas and fibrocalcific plaques, macrophages and foam cells become dysfunctional due to prolonged exposure to lipids and an inflammatory microenvironment[11,12]. In early PIT lesions, macrophages attempting to clear inflammatory lipids (for example, oxLDLs) accumulate excess cholesterol, and triglycerides within cytoplasmic lipid droplets[12] may be more prone to viral infection. SARS-CoV-2 showed a stronger tropism for the arterial lesions than corresponding perivascular fat, which was related to the degree of macrophage infiltration, consistent with the higher viral replication in PIT lesions and fibroatheromas, where macrophages are more prevalent. Others previously reported the presence of SARS-CoV-2 vRNA within the heart and the aorta as well as other distant organs[8,14,59,60]. Our data conclusively demonstrate that SARS-CoV-2 is capable of infecting and replicating in macrophages within the coronary vasculature of patients with COVID-19. Furthermore, SARS-CoV-2 preferentially replicates in foam cells compared to other macrophages, due to a reduced type I IFN response that leads to vRNA and viral protein accumulation, suggesting that these cells might act as a reservoir of SARS-CoV-2 viral debris in the atherosclerotic plaque. Our results demonstrate that, although type I IFN response remained elevated in SARS-CoV-2-infected macrophages, indicating a sustained antiviral state, infected foam cells exhibited only a transient expression of type I IFN gene expression. Together with the reduced expression of lysosomal genes and lower inflammatory response to SARS-CoV-2 infection, the reduced type I IFN may contribute to the persistence of SARS-CoV-2 observed in the analyzed atherosclerotic autopsy specimens. Macrophages residing in vascular tissue can undergo self-renewal, contributing to their long-term maintenance[61], and, in heart transplant studies, it has been shown that cardiac macrophages have a half-life of 8.8 years[62]. Therefore, it is possible that macrophages may act as reservoirs of SARS-CoV-2 vRNA in atherosclerotic plaques. We also identified infected VSMCs in coronary autopsy specimens. Although the number of infected VSMCs was lower than that of infected macrophages, VSMCs have a half-life of 270–400 d[63] and may contribute to SARS-CoV-2 persistence in the arterial wall.

SARS-CoV-2 infection of macrophages and foam cells promoted a strong inflammatory response characterized by release of cytokines implicated in both the pathogenesis of atherosclerosis and the increased risk of cardiovascular events, such as stroke and myocardial infarction[46,47,64]. Using an ex vivo model of viral infection of human vascular explants, we found that atherosclerotic tissue could be directly infected by SARS-CoV-2, confirming our observation in tissues of patients with COVID-19. As in cultured macrophages and foam cells, SARS-CoV-2 infection of vascular tissue triggered an inflammatory response and induced the secretion of key pro-atherogenic cytokines, such as IL-6 and IL-1β. Considering that plaque inflammation promotes

disease progression and contributes to plaque rupture, our results provide a molecular basis for how SARS-CoV-2 infection of coronary lesions can contribute to the acute cardiovascular manifestations of COVID-19, such as myocardial infarction[3,5]. SARS-CoV-2 infection of coronaries was unrelated to pre-existing clinical characteristics, stage of COVID-19 by illness days, duration of hospitalization at the time of death or comorbidities. However, we found a higher accumulation of SARS-CoV-2 S and S antisense vRNA in the coronary vasculature of the three patients with acute ischemic cardiovascular manifestations, including posterior myocardial infarction (Pt. 1) and type II myocardial infarction (Pt. 2 and Pt. 3). Although evidence of coronary occlusion was not detected at autopsy for two patients with clinical diagnosis of myocardial infarction, these data suggest that SARS-CoV-2 coronary infection may increase cardiovascular risk. A systematic analysis of GTEx, a multi-tissue gene expression dataset that includes donors who died from cerebrovascular disease (>22%) and heart disease (>40%), revealed a similar expression pattern of SARS-CoV-2 receptors and co-factors in the human vasculature as that found in the lungs. In particular, although *ACE2* expression was low in the aorta and the tibial artery, its expression levels in the coronary artery are similar to those in the lung, suggesting that the coronary vasculature may be more susceptible to SARS-CoV-2 viral infection than other vascular beds. At the single-cell level, expression of SARS-CoV-2 receptors and factors confirmed our coronary vasculature autopsy findings. Although *ACE2* expression was not detectable by scRNA-seq, *NRP1* and *FURIN* were highly expressed in two *TREM2*+ macrophage clusters, known to correspond to plaque foamy macrophages[56], as well as in clusters of *SSP1*+ macrophages and *LYVE1*+ macrophages. We further found that SARS-CoV-2 infects NRP1+ macrophages within human coronary tissue at autopsy and that viral replication was greater in NRP1+ macrophages present in PIT lesions. Experimentally, both silencing of *NRP1* gene and a specific inhibitor of the interaction between the b1 domain of NRP-1 and the SARS-CoV-2 S1 CendR[53,54] reduced SARS-CoV-2 infectivity of human primary macrophages and foam cells, confirming that SARS-CoV-2 infection of macrophage and foam cell is, in part, NRP-1 dependent. However, an aberrant pro-inflammatory response associated with NRP-1 inhibition limits the potential therapeutic use of NRP-1 inhibitor. This pro-inflammatory effect, although unexpected in the context of SARS-CoV-2 infection, is consistent with previous findings of a protective role of NRP-1 in sepsis and the increased release of pro-inflammatory cytokines (for example, IL-6) from NRP-1 null macrophages[58].

Overall, our data demonstrate that SARS-CoV-2 replicates in macrophages within human coronaries of patients who died from severe COVID-19. Our study is limited to the analysis of a small cohort of older individuals with COVID-19 and pre-existing atherosclerosis and other medical conditions and comorbidities. Therefore, our observations cannot be extrapolated to younger, healthy individuals. Our study is also limited to cases that occurred during the early phases of the COVID-19 pandemic, and the findings that SARS-CoV-2 replicates in the atherosclerotic coronary vasculature is pertinent only to the viral strains that circulated in New York City between May 2020 and May 2021. Despite these limitations, our study highlights the hyperinflammatory response orchestrated by SARS-CoV-2-infected plaque macrophages and foam cells as a mechanistic link between infection of atherosclerotic coronary vessels and acute cardiovascular complications of COVID-19.

Methods

Ethical approval for the use of human autopsy specimens was obtained from the institutional review board (IRB) of NYU Langone Health (NYULH) (IRB i21-01587) in compliance with all relevant ethical regulations. Patients undergoing CEA who signed a written informed consent were enrolled in the ATHERO-IN study approved by the IRBs of the Icahn School of Medicine at Mount Sinai (IRB 11–01427) and NYULH (IRB i21-00429). The reported demographic information and clinical history

are de-identified and covered by the patients' consent to publish such data in compliance with IRB 11–01427 and IRB i21-00429.

Coronary autopsy specimens from patients with COVID-19
Formalin-fixed, paraffin-embedded coronary artery specimens ($n = 27$) from eight deceased patients diagnosed with COVID-19 were obtained from NYULH and the NYU Grossman School of Medicine's Center for Biospecimen Research and Development (CBRD). Demographic information and clinical history were obtained from the hospital medical records (Supplementary Table 1). Data on the clinical course of the infection and COVID-19-associated pathology were obtained from both the hospital medical records and autopsy pathology reports (Supplementary Table 2).

RNAscope in situ hybridization
The RNAscope 4-plex assay was performed on coronary tissue sections using LS Multiplex Reagent Kit and RNAscope LS 4-plex Ancillary Kit (ACD Bio-Techne). SARS-CoV-2-specific RNAscope probes were used to visualize the SARS-CoV-2 vRNA encoding the S protein and to detect direct viral replication using a sense probe that targets the antisense strand of the S gene. Negative and positive control probes were used to assess tissue RNA integrity. RNAscope probes used for detecting *CD68*, *ACTA2* and *NRP1* transcripts, SARS-CoV-2 S viral gene, antisense strand of S gene and other reagents are detailed in Supplementary Table 5. Tissue sections were scanned at ×40 magnification in the Vectra Polaris Automated Quantitative Pathology Imaging System using a MOTIF workflow. For the in vitro experiments, human peripheral blood mononuclear cell-derived macrophages, macrophage-derived foam cells, primary aortic VSMCs and cholesterol-loaded VSMCs were infected with SARS-CoV-2 before performing RNAscope ISH Multiplex Fluorescent V2 Assay protocol according to the manufacturer's instructions. Images were acquired with a Keyence BZ-X800 microscope.

RNAscope in situ hybridization analysis
Images were annotated in Phenochart whole slide viewer (Akoya Biosciences). Whole slide scan '.qptiff' files were stamped for InForm batch on Phenochart (version 1.1). Spectral unmixing of all images was performed using InForm's automated algorithm. The stamped images were processed through InForm (PerkinElmer, version 2.6), and 'component_data.tif' files were exported for quantification using the HALO image analysis platform (version 3.5.3577) and HALO AI (version 3.6.4134) (Indica Labs) using the classifier module, neural network classifier module and spatial analysis module. The algorithms used were Area Quantification (version 2.4.2 and version 2.4.3), Area Quantification FL (version 2.3.3 and version 2.3.4), Deconvolution (version 1.1.7 and version 1.1.8) and FISH (version 3.2.3). AI was trained-by-example to classify the regions of the tissue. HALO AI trained Mininet deep learning classifier was used to classify the coronary wall and corresponding perivascular fat in all sections and to remove background autofluorescence. Cell segmentation was performed by training AI nuclei segmentation network classifier with DAPI-stained nuclei on both the stitched images of whole coronary tissue and in vitro experiments' images. Quantification of the probes was based on color and constant image intensity thresholding, maintaining parameters constant across samples. HALO imaging analysis algorithms and spatial analysis workflow were used to quantify the number of positive dots per cell and the frequency of positive cells divided by total cells.

IHC
H&E and chromogenic IHC were performed by the NYULH CBRD. IHC for the quantification of macrophages was performed on a Ventana Medical Systems Discovery Ultra platform using rabbit anti-human CD68 (ref. 65) (Ventana Medical Systems). Images were acquired in the Vectra Polaris multimodal digital pathology. Histopathology assessment and coronary pathology reports were performed by a blinded

clinical cardiovascular pathologist. Quantification of percentage of CD68$^+$ area was performed with the hybrid cell count module of the Keyence BZ-X800 microscope. CD68$^+$ cell count and frequency were obtained using HALO imaging analysis algorithms and AI nuclei segmentation.

Immunofluorescence
Autopsy coronary sections were stained with primary antibodies at 4 °C overnight and with secondary antibodies at room temperature for 2 h, and cell nuclei were stained with DAPI. Autofluorescence was quenched with TrueBlack Lipofuscin Autofluorescence Quencher (Biotium). Cultured macrophages and foam cells were stained with a mouse anti-SARS-CoV-2 NP antibody (ProScience) overnight at 4 °C, followed by a goat anti-mouse Alexa Fluor 488 (Invitrogen) for 2 h at room temperature. Images were acquired using a Keyence BZ-X800 microscope. Primary and secondary antibodies used are listed in Supplementary Table 5.

scRNA-seq of human carotid arteries
Carotid plaques were obtained from patients undergoing CEA ($n = 10$) enrolled in the Athero-IN study (IRB 11–01427 and IRB i21-00429). Exclusion criteria for patient enrollment were as follows: active infection, autoimmune diseases, active or recurrent cancer and severe renal failure requiring dialysis. Supplementary Table 4 summarizes the clinical and demographic characteristics of the study cohort. Plaques were classified by a clinical cardiovascular pathologist (N.N.) as fibrocalcific ($n = 3$) and fibroatheroma ($n = 4$). Three of 10 plaque tissues were not classified owing to insufficient tissue.

Cell isolation from carotid atherosclerotic tissues
Fresh plaque specimens were placed immediately in DMEM (Gibco) and processed within 30 min to obtain single-cell suspension using a digestion protocol previously described[66]. In brief, the specimens were washed and digested in DMEM containing 10% FBS (Gibco, 10082147); collagenase type IV (Sigma-Aldrich, C5138) at a final concentration of 1 mg ml^{-1}; and DNase I (Sigma-Aldrich, DN25), hyaluronidase (Sigma-Aldrich, H3506), collagenase type XI (Sigma-Aldrich, C7657) and collagenase type II (Sigma-Aldrich, C6885), each at a final concentration of 0.3 mg ml^{-1} for 40 min in a gentleMACS Octo Dissociator (Miltenyi Biotec). The digested tissue was sequentially filtered through 70-μm and 40-μm cell strainers (Thermo Fisher Scientific, 22363547 and 22363548) and centrifuged at 300g for 8 min. Dead cells were removed with the EasySep Dead Cell Removal (Annexin V) Kit (STEMCELL Technologies, 17899), and leukocytes were isolated with the EasySep Release Human CD45 Positive Selection Kit (STEMCELL Technologies, 100-0105) according to the manufacturer's instructions. Live cells were counted with the automatic cell counter Cellometer Auto 2000 (Nexcelom), and cells were loaded to the Chromium Controller (10x Genomics). scRNA-seq libraries were prepared using the Chromium Single Cell 3′ Library v3 reagent, Gel Bead and Multiplex Kit and Chip Kit (10x Genomics). DNA library quantity and quality were measured with Qubit dsDNA HS fluorometric assay (Qiagen) and Bioanalyzer (Agilent) and sequenced on a NovaSeq 6000 sequencer (Illumina). scRNA-seq data from six samples were previously published[66] and are available in the GEO (GSE224273). Four extra samples were processed to obtain additional scRNA-seq data (GEO: GSE235437).

Computational analysis of coronary and carotid scRNA-seq
Cell Ranger Single-Cell Software Suite (version 3.1.0) was used to demultiplex and align to the human genome reference version GRCh38. A total of 20,639 CD45$^+$ cells were analyzed as were Cell Ranger outputs from the CEA scRNA-seq data with an average of 104,351 mean reads per cell and 3,128 median unique molecular identifier (UMI) counts per cell. An scRNA-seq dataset (GSE131780) comprising human atherosclerotic coronary samples was obtained from the GEO dataset repository[15].

A total of 12,200 coronary cells from seven tissue samples obtained from four patients were analyzed. Cell Ranger outputs had an average of 62,328 mean reads per cell and 2,703 median UMI counts per cell.

The output filtered gene expression matrices were analyzed using the Seurat package (version 4.0.3)[67]. Mitochondrial genes >10% to >20%, <200 genes and <10,000 to <20,000 UMIs were filtered out. Gene expression matrices were normalized using the SCTransform function, and robust principal component analysis was used for integration. The RunPCA function was used to compute the top 30 principal components using variably expressed genes. FindIntegrationAnchors served to identify anchors between carotid samples and were inputted into the IntegrateData function to correct for batch effects. Cells were assigned a cell cycle score using the CellCycleScoring function to regress out unwanted variation. RunUMAP with FindNeighbors and FindClusters functions were used for cell clustering. Integration/co-clustering of carotid and coronary single cells was performed using Harmony[68]. The dimensionality reduction generated by Harmony was used to calculate uniform manifold approximation and projection (UMAP) and graph-based clustering with a resolution of 0.7. FindAllMarkers was used to find differentially expressed genes (DEGs) using the Wilcoxon rank-sum statistical test, and major cell populations were annotated using DEGs and canonical marker genes. Subclustering analysis of myeloid cells was performed with same approach described above. MiloR package (version 1.3.1)[55] was used to test for differential abundance between carotid and coronary. Cell neighborhoods were defined on a k-nearest neighbor (kNN) graph ($k = 20$, $d = 30$), and testing for differential abundance was done using a negative binomial general linear model framework. Cell neighborhoods were annotated to their clusters, and differential abundance was expressed as log fold changes (FCs) displayed in a beeswarm plot.

GTEx dataset analysis
Gene expression analysis of SARS-CoV-2 entry factors in aorta, coronary and tibial arteries, heart (atrial appendage and left ventricle), lung and whole blood was performed using GTEx data (version V8, dbGaP accession number phs000424.v8.p2), which contains 17,382 RNA-seq tissue samples in total from 948 deceased donors (67.1% males). The cohort includes Caucasian (84.6%), African American (12.9%), American Indian (0.2%), Asian (1.3%) and unknown (1.1%) ancestry. The registered causes of death are traumatic injury, cerebrovascular disease (>22%) or heart disease (>40%). Results are shown as a logarithmic scale of transcripts per million ($\log_{10} \mathrm{TMP^{+1}}$).

Computational analysis of murine scRNA-seq data
Sequencing data from ref. 16 were extracted from BioProject accession number PRJNA626450. Quality control of scRNA-seq data was performed using FastQC (version 0.11.7). Reads were aligned to the GRCm39 (mm39) reference genome using STAR (version 2.6.1d). FeatureCounts from the subread package (version 1.6.3) was employed and normalized counts used for downstream analysis using the Seurat R package (version 4.3.0). Highly variable genes were identified using the FindVariableFeatures function. RunUMAP function with default settings was used with FindNeighbors and FindClusters functions for cell clustering. Differential gene expression analysis was performed using the FindMarkers function to identify differences between single-color Tomato reporter (Myh11-CreERT2, Rosa26tdTomato/tdTomato, ApoE$^{-/-}$ mice) fed a high-fat diet (21% anhydrous milk fat, 19% casein and 0.25% cholesterol) for 18 weeks versus control mice. The Benjamini–Hochberg method was applied to control for the false discovery rate (FDR).

Experiments in Biosafety Level 3
Studies involving SARS-CoV-2 infection were approved by the Institutional Biosafety Committee (IBC21-000079) of the NYU Grossman School of Medicine. All Biosafety Level 3 procedures were conducted in accordance with the Biosafety Manual and standard operating procedures of the NYU Grossman School of Medicine High-Containment Facility.

Cells and viruses
Vero E6 cells (American Type Culture Collection, CRL-1586) were maintained in DMEM culture media containing 10% FBS (Gibco), 2 mM L-glutamine and 100 U ml^{-1} penicillin–streptomycin. Vero E6 Expressing Transmembrane Protease, Serine 2 and Human Angiotensin-Converting Enzyme 2 (Vero E6-TMPRSS2-T2A-ACE2) were obtained from BEI Resources (NR-54970). Vero E6-TMPRSS2-T2A-ACE2 cells were grown in DMEM medium with 4 mM L-glutamine, 4,500 ml of glucose, 1 mM sodium pyruvate and 1,500 mg L^{-1} sodium bicarbonate, 10% FBS and 10 µg ml^{-1} puromycin. All cells were verified to be free of mycoplasma contamination.

SARS-CoV-2 isolate USA-WA1/2020 (BEI Resources, NR52281) was amplified once in Vero E6 cells infected at a multiplicity of infection (MOI) of 0.01 as previously described[69]. Virus was collected at 72 hpi upon observation of cytopathic effect. Debris was removed by centrifugation and passage through a 0.22-µm filter, and the supernatant was then aliquoted and stored at −80 °C. Virus titer was calculated by plaque assay on Vero E6 cells and informed as particle-forming units per milliliter (PFU ml^{-1}). Virus stocks were Sanger sequenced during viral stock production. A PCR amplicon covering the S gene (FW: gttcagagtttattctagtgcgaataattgcactttg, RV: gcagtaaggatggctagtgtaactagcaagaataccac) was purified using the Nucleospin PCR and Gel Extraction Kit (Macherey-Nagel) and Sanger sequenced (GENEWIZ) with the following primers (FW: ggttttaattgttactttcc and FW: ctacaggttctaatgtttttc). icSARS-CoV-2 mNG reporter virus was obtained from the UTMB World Reference Center for Emerging Viruses and Arboviruses[21].

In vitro SARS-CoV-2 infection of human primary cells
Human primary monocytes were differentiated into macrophages in the presence of 20 nM human macrophage colony-stimulating factor (M-CSF, PeproTech) in DMEM culture media supplemented with 10% FBS, 2 mM L-glutamine and 100 U ml^{-1} penicillin–streptomycin for 5 d. Macrophages were then treated with 10 µg ml^{-1} of either Dil-oxLDL or ox-LDL (Invitrogen) for 1 h before infection and kept throughout the experiment. Human aortic smooth muscle cells (PromoCell, C-12533) were cultured in complete Smooth Muscle Cell Growth Medium with 0.05 ml/ml FCS, 0.5 ng ml^{-1} recombinant human epidermal growth factor, 0.2 ng ml^{-1} recombinant human basic fibroblast growth factor and 5 µg ml^{-1} recombinant human insulin and treated with 10 µg ml^{-1} Cholesterol–methyl-β-cyclodextrin (Sigma-Aldrich) overnight before infection with SARS-CoV-2 virus USA-WA1/2020 isolate at MOI 0.1 in infection media with 2% FBS. Mock-infected cells were used as controls. Cell culture supernatants were inactivated with UV irradiation for 15 min and stored at −80°C. Cells were collected in either TRIzol (Invitrogen) or 10% buffered formalin. Macrophages and foam cells were treated with EG00229 trifluoroacetate (Tocris, 6986) at 100 µM final concentration for 1 h before infection.

Lipid staining with Oil Red O
VSMCs treated with 10 µg ml^{-1} of Cholesterol–methyl-β-cyclodextrin or vehicle for 48 h were fixed with 10% buffered formalin for 1 h and incubated with 60% isopropanol for 1 min. Staining with Oil Red O (Sigma-Aldrich) working solution was performed for 20 min before hematoxylin counterstain for 1 min. Images were acquired with a Keyence BZ-X800 microscope.

Ex vivo SARS-CoV-2 infection of human vascular explants
Carotid plaque specimens were thawed, cut into pieces (approximately 3 × 3 mm) and cultured in DMEM culture media supplemented with 10% FBS, 2 mM L-glutamine and 100 U ml^{-1} penicillin–streptomycin for 2 h. Tissue specimens were infected with 10^5 PFU ml^{-1} of SARS-CoV-2 virus

USA-WA1/2020 isolate. Non-infected tissues were used as controls. Culture media samples were collected at 24 hpi, 48 hpi and 72 hpi and inactivated by UV irradiation for 15 min. Tissue specimens were fixed overnight with either 4% paraformaldehyde for immunofluorescence or 3% glutaraldehyde for electron microscopy. Tissues used for bulk RNA-seq were stored in 1 ml of TRIzol reagent. For NRP-1 blocking experiments, tissues were pre-treated with NRP1 blocking agent (EG00229 trifluoroacetate) at a final concentration of 100 µM for 1 h before infection.

Infectious particle quantification by plaque assay

Ten-fold dilutions of conditioned culture media were added to Vero E6-TMPRSS2-T2A-ACE2 cell monolayers for 1 h and gently shaken every 15 min. After incubation, cells were overlaid with 0.8% agarose in DMEM containing 2% FBS and incubated for 36 h. After fixation, agarose plugs were removed, and plaques were visualized by crystal violet solution staining. Plaques were counted, and the results were expressed as PFU ml^{-1}. Plaque assays using Vero E6 cells were performed with a 72-h incubation period.

Silencing of NRP1 in human macrophages and foam cells

Transient knockdown of NRP1 was achieved using a pool of pre-designed siRNA FlexiTube GeneSolution for NRP1 silencing (Qiagen, GS8829; Hs_NRP1_8, ACGGTCATAGACAGCACCATA; Hs_NRP1_7, CACGCGATTCATCAGGATCTA; Hs_NRP1_12, ACAGCCT TGAATGCACT-TATA; Hs_NRP1_11, CTCCCAGATCACATCATCCAA) and non-targeting negative control (Qiagen, AllStars Negative Control siRNA). In brief, 3 µl of Lipofectamine RNAiMAX (Invitrogen) and siRNA oligos 10 nM final concentration were added to a final volume of 200 µl of OptiMEM reduced serum medium (Gibco). The mix was incubated at room temperature for 20 min. Plated cells (60–80% confluence) were transfected by adding oligos/Lipofectamine RNAiMAX complexes in a final volume of 1 ml with DMEM without serum or antibiotics overnight (-16 h) before replacing the medium with complete DMEM medium with 10% FBS for 24 h. After 24 h, half of the cells were treated with 10 µg ml^{-1} oxLDL for 2 h before infection with SARS-CoV-2 virus USAWA1/2020 isolate MOI 0.1 in infection media (2% FBS DMEM) for 24 h. Cells were harvested for RNA and protein analysis, and cell culture supernatants were UV inactivated for 15 min. Cells were fixed with 10% buffered formalin for 1 h before RNAscope staining.

Protein quantification and western blot analysis

Protein lysates, obtained using RIPA buffer containing phosphatase and protease inhibitor cocktail (100×), were processed to quantify protein concentration using the Pierce BCA Protein Assay Kit. The following antibodies were used for western blot analysis: anti-NRP1 rabbit monoclonal antibody (Cell Signaling Technology), anti-β-actin mouse monoclonal antibody (Sigma-Aldrich) and anti-rabbit and anti-mouse HRP-conjugated secondary antibodies (ProteinSimple). All reagent information is listed in Supplementary Table 5. Molecular weight markers and samples were run through the ProteinSimple WES System, and images were analyzed using the Compass for Simple Western software (version 6.2.0).

RT–qPCR

RNA was extracted using TRIzol reagent and Direct-zol RNA Microprep Kits (Zymo Research) or RNAeasy Mini Kit (Qiagen). Reverse transcription (High-Capacity cDNA Reverse Transcription Kit, Applied Biosystems) was carried out at 37 °C for 1 h, and the reaction was stopped by heating to 95 °C for 5 min and hold at 4 °C. RT–qPCR was performed using gene-specific primers (Supplementary Table 5) using the TaqMan Fast Advanced Master Mix and the Applied Biosystems QuantStudio 6 Pro detection system. The thermal cycling conditions were 50 °C for 2 min, followed by a step at 95 °C for 2 min and 40 cycles at 95 °C for 1 s and 60 °C for 20 s. The relative quantification of the SARS-CoV-2

NP gene was calculated using the $2^{-\Delta\Delta Ct}$ method in Design and Analysis Software version 2.6. FCs in gene expression were normalized to housekeeping control gene and calculated log$_{10}$FC relative to control sample (2 h after viral inoculum). For NRP1 silencing in vitro experiments quality control, FCs in gene expression of the *NRP1* target gene were normalized to the *GAPDH* housekeeping control gene. Relative quantification was performed using the $2^{-\Delta\Delta Ct}$ method, and samples were normalized by the endogenous controls.

Bulk RNA-seq

RNA from primary macrophages and foam cells was extracted using TRIzol reagent and Direct-zol RNA Microprep Kits following the manufacturer's instructions. Total RNA from human atherosclerotic tissue was isolated using QIAzol Lysis Reagent (Qiagen) and the gentleMACS Octo Dissociator (Miltenyi Biotec) homogenizer, combined with RNA cleanup using the RNAeasy Mini Kit (Qiagen). Quality control was performed with Agilent RNA 6000 Nano and Pico Kits (Agilent Technologies) using the Agilent 2100 Bioanalyzer system. For in vitro experiments, poly(A) library preparation was performed using Illumina Stranded mRNA Preparation and Ligation (Illumina). For human atherosclerotic plaque ex vivo experiments, the Revelo RNA-Seq High Sensitivity library preparation kit was used (Tecan). Libraries were quantified using KAPA Library Quantification Kit (Roche), pooled at 2 nM equimolar concentration and sequenced using an Illumina NovaSeq 6000 sequencer.

RNA-seq data processing, analysis and visualization

Quality control of RNA-seq data was performed using FastQC2 (version 0.11.7). Raw sequenced reads were trimmed using fastp3 (version 0.20.1) for quality control of bases and to eliminate sequencing adaptors. Raw reads were aligned using STAR (version 2.6.1d) to the combined human (*Homo sapiens*) genome assembly GRCh38 from the Genome Reference Consortium (GCA_000001405.15 GCF_000001405.26) and SARS-CoV-2 Washington isolate (USA WA1/2020) genome (GenBank: MN985325.1). The gene-level expression counts were computed with the featureCounts function in the Subread package (version 1.6.3; parameters: -g gene_id -s 2) using the human gene annotations from GENCODE release 33. Differential expression was performed using the R package DESeq2 (version 1.30.1). To model differences in gene expression between SARS-CoV-2-infected versus non-infected primary macrophages and foam cells, a model including infection status, timepoint and donor as dependent variables was used. To identify differences in gene expression between infected macrophages and infected foam cells, a model including cell type, timepoint and donor as dependent variables was used. To analyze gene expression variation across timepoints and infection status in macrophages and foam cells, we employed a model that incorporated infection status, timepoint, donor and an interaction between infection status and timepoint as dependent variables for each sample type separately. The IFN and SARS-CoV-2 scores were calculated as log$_2$ values of IFN response genes and SARS-CoV-2 genes comparing macrophage and foam cell response at 0 hpi, 2 hpi, 8 hpi, 24 hpi and 48 hpi. Standardized data (z-scores) were calculated for each feature by subtracting the estimate mean and dividing by the estimate s.d. For hierarchical clustering, data were plotted using the pheatmap package (version 1.0.12) in R. Differential expression analysis of SARS-CoV-2-infected atherosclerotic plaque samples was performed using the R package DESeq2 with timepoint and donor included as dependent variables. For hierarchical clustering analysis, normalized values were standardized and plotted using the pheatmap package (version 1.0.12) in R. *P* values were adjusted using Benjamini–Hochberg correction and denoted as an asterisk. Gene set enrichment analysis using Reactome Knowledgebase 2022 and Gene Ontology Biological Process 2021 of the top 300 DEGs was performed using Enrichr (https://maayanlab.

cloud/Enrichr/)[70,71]. Bar plots represent the combined score of 10 top relevant pathways with statistical significance (*$P < 0.05$, **$P < 0.01$; ***$P < 0.001$).

Cytokine and chemokine protein secretion

A screen of 48 human cytokines and chemokines was performed using UV-inactivated culture supernatants by using the Bio-Plex Pro Human Cytokine Screening Panel (Bio-Rad) and the Luminex 200 platform of the Immune Monitoring Laboratory Division of Advanced Research Technologies of the NYU Grossman School of Medicine. Luminex data were log transformed; statistically significant differences were calculated using unpaired two-sided t-tests; and P values were adjusted using Benjamini–Hochberg correction. Empirical Bayes batch correction (Combat) was used to remove batch effects before log transforming the data. Statistical analysis was performed using R (version 4.0.3). Cytokines showing $\log_2FC > 0$ were upregulated, and cytokines showing $\log_2FC < 0$ were downregulated. Secreted TGF-β1 and Caspase-8 were measured by ELISA (Invitrogen) in clarified culture media supernatant, according to the manufacturer's instructions.

Transmission electron microscopy

After 48 hpi and 72 hpi, ex vivo SARS-CoV-2-infected atherosclerotic samples were fixed with 3% glutaraldehyde/PBS (pH 7.4) at 4 °C. Samples were prepared for electron microscopic evaluation by the NYU Grossman School of Medicine's Microscopy Laboratory following standard operating procedures. The specimens were examined by transmission electron microscopy. Stained grids were imaged with a Talos L120C transmission electron microscope and recorded using a Gatan OneView Camera (4 K × 4 K resolution) with Digital Micrograph software (Gatan Microscopy Suite).

Statistical analysis

Statistical analyses not described above were performed using GraphPad Prism version 9.0, and details are included in the figure legends. Statistical P values were calculated and reported on graphs, and $P < 0.05$ was considered significant.

Reporting summary

Further information on research design is available in the Nature Portfolio Reporting Summary linked to this article.

Data availability

scRNA-seq data from the six human carotid arteries were previously published and are available in the GEO (GSE224273). Four additional carotid plaques were processed to obtain sc-RNAseq data deposited in the GEO (GSE235437). scRNA-seq data coronary lesions were obtained from the GEO (GSE131780). Bulk RNA-seq data from macrophages and foam cell experiments and the plaque tissues infected with SARS-CoV-2 are deposited in the GEO (GSE235437). GTEx data used are version V8, dbGaP accession number phs000424.v8.p2, and available at the GTEx portal (https://gtexportal.org/home). Murine scRNA-seq data from ref. 16 were extracted from BioProject accession number PRJNA626450. Human (*Homo sapiens*) genome assembly GRCh38 (hg38) was obtained from the Genome Reference Consortium (GCA_000001405.15 GCF_000001405.26). SARS-CoV-2 Washington isolate (WA1/2020) genome was obtained from the NIH repository (GenBank: MN985325.1). The following reagent was deposited by the Centers for Disease Control and Prevention and obtained through BEI Resources, NIAID, NIH: SARS-Related Coronavirus 2, Isolate hCoV-19/USA-WA1/2020, NR-52281. The following reagent was obtained through BEI Resources, NIAID, NIH *Cercopithecus aethiops* Kidney Epithelial Cells Expressing Transmembrane Protease, Serine and Human Angiotensin-Converting Enzyme 2 (Vero E6-TMPRSS2-T2A-ACE2, NR-54970). All other data supporting the findings in this study are included in the main article and associated files. Source data files are available on GitHub at https://github.com/giannarelli-lab/SARS-CoV-2-infection-triggers-pro-atherogenic-inflammatory-responses-in-human-coronary-vessels.

Code availability

Code used for data analysis is available on GitHub at https://github.com/giannarelli-lab/SARS-CoV-2-infection-triggers-pro-atherogenic-inflammatory-responses-in-human-coronary-vessels.

References

1. Lamers, M. M. & Haagmans, B. L. SARS-CoV-2 pathogenesis. *Nat. Rev. Microbiol.* **20**, 270–284 (2022).
2. Engelen, S. E., Robinson, A. J. B., Zurke, Y. X. & Monaco, C. Therapeutic strategies targeting inflammation and immunity in atherosclerosis: how to proceed? *Nat. Rev. Cardiol.* **19**, 522–542 (2022).
3. Katsoularis, I., Fonseca-Rodriguez, O., Farrington, P., Lindmark, K. & Fors Connolly, A. M. Risk of acute myocardial infarction and ischaemic stroke following COVID-19 in Sweden: a self-controlled case series and matched cohort study. *Lancet* **398**, 599–607 (2021).
4. Kwong, J. C. et al. Acute myocardial infarction after laboratory-confirmed influenza infection. *N. Engl. J. Med.* **378**, 345–353 (2018).
5. Merkler, A. E. et al. Risk of ischemic stroke in patients with Coronavirus Disease 2019 (COVID-19) vs patients with influenza. *JAMA Neurol.* **77**, 1366–1372 (2020).
6. Xie, Y., Xu, E., Bowe, B. & Al-Aly, Z. Long-term cardiovascular outcomes of COVID-19. *Nat. Med.* **28**, 583–590 (2022).
7. Fajgenbaum, D. C. & June, C. H. Cytokine storm. *N. Engl. J. Med.* **383**, 2255–2273 (2020).
8. Liu, J. et al. SARS-CoV-2 cell tropism and multiorgan infection. *Cell Discov.* **7**, 17 (2021).
9. Sefik, E. et al. Inflammasome activation in infected macrophages drives COVID-19 pathology. *Nature* **606**, 585–593 (2022).
10. Moore, K. J., Sheedy, F. J. & Fisher, E. A. Macrophages in atherosclerosis: a dynamic balance. *Nat. Rev. Immunol.* **13**, 709–721 (2013).
11. Narula, N., Olin, J. W. & Narula, N. Pathologic disparities between peripheral artery disease and coronary artery disease. *Arterioscler. Thromb. Vasc. Biol.* **40**, 1982–1989 (2020).
12. Otsuka, F. et al. Natural progression of atherosclerosis from pathologic intimal thickening to late fibroatheroma in human coronary arteries: a pathology study. *Atherosclerosis* **241**, 772–782 (2015).
13. Saccon, T. D. et al. SARS-CoV-2 infects adipose tissue in a fat depot- and viral lineage-dependent manner. *Nat. Commun.* **13**, 5722 (2022).
14. Martinez-Colon, G. J. et al. SARS-CoV-2 infection drives an inflammatory response in human adipose tissue through infection of adipocytes and macrophages. *Sci. Transl. Med.* **14**, eabm9151 (2022).
15. Wirka, R. C. et al. Atheroprotective roles of smooth muscle cell phenotypic modulation and the TCF21 disease gene as revealed by single-cell analysis. *Nat. Med.* **25**, 1280–1289 (2019).
16. Wang, Y. et al. Clonally expanding smooth muscle cells promote atherosclerosis by escaping efferocytosis and activating the complement cascade. *Proc. Natl Acad. Sci. USA* **117**, 15818–15826 (2020).
17. Rong, J. X., Shapiro, M., Trogan, E. & Fisher, E. A. Transdifferentiation of mouse aortic smooth muscle cells to a macrophage-like state after cholesterol loading. *Proc. Natl Acad. Sci. USA* **100**, 13531–13536 (2003).
18. Shankman, L. S. et al. KLF4-dependent phenotypic modulation of smooth muscle cells has a key role in atherosclerotic plaque pathogenesis. *Nat. Med.* **21**, 628–637 (2015).

19. Feil, S. et al. Transdifferentiation of vascular smooth muscle cells to macrophage-like cells during atherogenesis. *Circ. Res.* **115**, 662–667 (2014).

20. Allahverdian, S., Chehroudi, A. C., McManus, B. M., Abraham, T. & Francis, G. A. Contribution of intimal smooth muscle cells to cholesterol accumulation and macrophage-like cells in human atherosclerosis. *Circulation* **129**, 1551–1559 (2014).

21. Xie, X. et al. An infectious cDNA clone of SARS-CoV-2. *Cell Host Microbe* **27**, 841–848 (2020).

22. Combe, M., Garijo, R., Geller, R., Cuevas, J. M. & Sanjuan, R. Single-cell analysis of RNA virus infection identifies multiple genetically diverse viral genomes within single infectious units. *Cell Host Microbe* **18**, 424–432 (2015).

23. Heldt, F. S., Kupke, S. Y., Dorl, S., Reichl, U. & Frensing, T. Single-cell analysis and stochastic modelling unveil large cell-to-cell variability in influenza A virus infection. *Nat. Commun.* **6**, 8938 (2015).

24. Zhu, Y., Yongky, A. & Yin, J. Growth of an RNA virus in single cells reveals a broad fitness distribution. *Virology* **385**, 39–46 (2009).

25. Cohen, E. M., Avital, N., Shamay, M. & Kobiler, O. Abortive herpes simplex virus infection of nonneuronal cells results in quiescent viral genomes that can reactivate. *Proc. Natl Acad. Sci. USA* **117**, 635–640 (2020).

26. Ioannidis, L. J., Verity, E. E., Crawford, S., Rockman, S. P. & Brown, L. E. Abortive replication of influenza virus in mouse dendritic cells. *J. Virol.* **86**, 5922–5925 (2012).

27. Lucas, C. et al. Longitudinal analyses reveal immunological misfiring in severe COVID-19. *Nature* **584**, 463–469 (2020).

28. Munnur, D. et al. Altered ISGylation drives aberrant macrophage-dependent immune responses during SARS-CoV-2 infection. *Nat. Immunol.* **22**, 1416–1427 (2021).

29. Cheng, J. et al. IL-27 induces IFN/STAT1-dependent genes and enhances function of TIGIT$^+$ HIVGag-specific T cells. *iScience* **25**, 103588 (2022).

30. Heaton, N. S. & Randall, G. Multifaceted roles for lipids in viral infection. *Trends Microbiol* **19**, 368–375 (2011).

31. Cloherty, A. P. M., Olmstead, A. D., Ribeiro, C. M. S. & Jean, F. Hijacking of lipid droplets by hepatitis C, dengue and Zika viruses—from viral protein moonlighting to extracellular release. *Int. J. Mol. Sci.* **21**, 7901 (2020).

32. Theken, K. N., Tang, S. Y., Sengupta, S. & FitzGerald, G. A. The roles of lipids in SARS-CoV-2 viral replication and the host immune response. *J. Lipid Res.* **62**, 100129 (2021).

33. Collins, K. L., Chen, B. K., Kalams, S. A., Walker, B. D. & Baltimore, D. HIV-1 Nef protein protects infected primary cells against killing by cytotoxic T lymphocytes. *Nature* **391**, 397–401 (1998).

34. Hansen, T. H. & Bouvier, M. MHC class I antigen presentation: learning from viral evasion strategies. *Nat. Rev. Immunol.* **9**, 503–513 (2009).

35. Bizzotto, J. et al. SARS-CoV-2 infection boosts MX1 antiviral effector in COVID-19 patients. *iScience* **23**, 101585 (2020).

36. Domizio, J. D. et al. The cGAS–STING pathway drives type I IFN immunopathology in COVID-19. *Nature* **603**, 145–151 (2022).

37. Prelli Bozzo, C. et al. IFITM proteins promote SARS-CoV-2 infection and are targets for virus inhibition in vitro. *Nat. Commun.* **12**, 4584 (2021).

38. Kuznetsova, T., Prange, K. H. M., Glass, C. K. & de Winther, M. P. J. Transcriptional and epigenetic regulation of macrophages in atherosclerosis. *Nat. Rev. Cardiol.* **17**, 216–228 (2020).

39. Seth, R. B., Sun, L., Ea, C. K. & Chen, Z. J. Identification and characterization of MAVS, a mitochondrial antiviral signaling protein that activates NF-κB and IRF 3. *Cell* **122**, 669–682 (2005).

40. Minkoff, J. M. & tenOever, B. Innate immune evasion strategies of SARS-CoV-2. *Nat. Rev. Microbiol.* **21**, 178–194 (2023).

41. Garcia-Nicolas, O., Godel, A., Zimmer, G. & Summerfield, A. Macrophage phagocytosis of SARS-CoV-2-infected cells mediates potent plasmacytoid dendritic cell activation. *Cell. Mol. Immunol.* **20**, 835–849 (2023).

42. Janeway, C. A.Jr & Medzhitov, R. Innate immune recognition. *Annu. Rev. Immunol.* **20**, 197–216 (2002).

43. tenOever, B. R. The evolution of antiviral defense systems. *Cell Host Microbe* **19**, 142–149 (2016).

44. Blanco-Melo, D. et al. Imbalanced host response to SARS-CoV-2 drives development of COVID-19. *Cell* **181**, 1036–1045 (2020).

45. Lazear, H. M., Schoggins, J. W. & Diamond, M. S. Shared and distinct functions of type I and type III interferons. *Immunity* **50**, 907–923 (2019).

46. Ridker, P. M. & Rane, M. Interleukin-6 signaling and anti-interleukin-6 therapeutics in cardiovascular disease. *Circ. Res.* **128**, 1728–1746 (2021).

47. Ridker, P. M. et al. Antiinflammatory therapy with canakinumab for atherosclerotic disease. *N. Engl. J. Med.* **377**, 1119–1131 (2017).

48. Zernecke, A., Bernhagen, J. & Weber, C. Macrophage migration inhibitory factor in cardiovascular disease. *Circulation* **117**, 1594–1602 (2008).

49. Wang, J. et al. Interleukin 18 function in atherosclerosis is mediated by the interleukin 18 receptor and the Na-Cl co-transporter. *Nat. Med.* **21**, 820–826 (2015).

50. Bastard, P. et al. Autoantibodies against type I IFNs in patients with life-threatening COVID-19. *Science* **370**, eabd4585 (2020).

51. Hoffmann, M. et al. SARS-CoV-2 cell entry depends on ACE2 and TMPRSS2 and is blocked by a clinically proven protease inhibitor. *Cell* **181**, 271–280 (2020).

52. Kyrou, I., Randeva, H. S., Spandidos, D. A. & Karteris, E. Not only ACE2—the quest for additional host cell mediators of SARS-CoV-2 infection: neuropilin-1 (NRP1) as a novel SARS-CoV-2 host cell entry mediator implicated in COVID-19. *Signal Transduct. Target. Ther.* **6**, 21 (2021).

53. Cantuti-Castelvetri, L. et al. Neuropilin-1 facilitates SARS-CoV-2 cell entry and infectivity. *Science* **370**, 856–860 (2020).

54. Daly, J. L. et al. Neuropilin-1 is a host factor for SARS-CoV-2 infection. *Science* **370**, 861–865 (2020).

55. Dann, E., Henderson, N. C., Teichmann, S. A., Morgan, M. D. & Marioni, J. C. Differential abundance testing on single-cell data using *k*-nearest neighbor graphs. *Nat. Biotechnol.* **40**, 245–253 (2022).

56. Kim, K. et al. Transcriptome analysis reveals nonfoamy rather than foamy plaque macrophages are proinflammatory in atherosclerotic murine models. *Circ. Res.* **123**, 1127–1142 (2018).

57. Solomon, B. D., Mueller, C., Chae, W. J., Alabanza, L. M. & Bynoe, M. S. Neuropilin-1 attenuates autoreactivity in experimental autoimmune encephalomyelitis. *Proc. Natl Acad. Sci. USA* **108**, 2040–2045 (2011).

58. Dai, X. et al. A novel role for myeloid cell-specific neuropilin 1 in mitigating sepsis. *FASEB J.* **31**, 2881–2892 (2017).

59. Stein, S. R. et al. SARS-CoV-2 infection and persistence in the human body and brain at autopsy. *Nature* **612**, 758–763 (2022).

60. Lindner, D. et al. Association of cardiac infection with SARS-CoV-2 in confirmed COVID-19 autopsy cases. *JAMA Cardiol.* **5**, 1281–1285 (2020).

61. Robbins, C. S. et al. Local proliferation dominates lesional macrophage accumulation in atherosclerosis. *Nat. Med.* **19**, 1166–1172 (2013).

62. Bajpai, G. et al. The human heart contains distinct macrophage subsets with divergent origins and functions. *Nat. Med.* **24**, 1234–1245 (2018).

63. Brewer, C. M. & Majesky, M. W. Branch point smooth muscle cells highlighted by novel lineage tracking approach. *Circ. Res.* **122**, 194–196 (2018).

64. Nilsson-Payant, B. E. et al. The NF-κB transcriptional footprint is essential for SARS-CoV-2 replication. *J. Virol.* **95**, e0125721 (2021).

65. Wang, S. et al. Programmed death ligand 1 expression and tumor infiltrating lymphocytes in neurofibromatosis type 1 and 2 associated tumors. *J. Neurooncol.* **138**, 183–190 (2018).

66. Fernandez, D. M. et al. Single-cell immune landscape of human atherosclerotic plaques. *Nat. Med.* **25**, 1576–1588 (2019).

67. Hao, Y. et al. Integrated analysis of multimodal single-cell data. *Cell* **184**, 3573–3587 (2021).

68. Korsunsky, I. et al. Fast, sensitive and accurate integration of single-cell data with Harmony. *Nat. Methods* **16**, 1289–1296 (2019).

69. Noval, M. G. et al. Antibody isotype diversity against SARS-CoV-2 is associated with differential serum neutralization capacities. *Sci Rep.* **11**, 5538 (2021).

70. Kuleshov, M. V. et al. Enrichr: a comprehensive gene set enrichment analysis web server 2016 update. *Nucleic Acids Res.* **44**, W90–W97 (2016).

71. Chen, E. Y. et al. Enrichr: interactive and collaborative HTML5 gene list enrichment analysis tool. *BMC Bioinformatics.* **14**, 128 (2013).

Acknowledgements

Author contributions

Conceptualization: N.E. and C.G. Methodology: N.E., M.G.N., O.S., R.K., K.M, K.A.S., N.N. and L.A. Biosafety Level 3 experiments: N.E., M.G.N. and S.J. Other experiments: M.S., N.E., O.S, B.C., L.A., D.D. and A.V.G. Patient recruitment: R.S., S.S. and D.F. Clinical data management: N.E., S.S., J.N., N.N., R.S., P.F. and A.R. Human sample collection: P.F., N.N., A.R., T.M. and C.R. Human sample processing: N.E., L.A., A.R., D.F., B.C. and D.D. Data analysis: N.E., D.D., M.G.N., R.K., M.G., D.F., J.N., B.C., D.D. and L.A. Resources: C.G., K.A.S. and A.R. Data visualization: N.E., R.K., M.G. and L.A. Writing—original draft: N.E. and C.G. Writing—revision and editing: all authors. Supervision: C.G. Project administration and funding acquisition: C.G.

Competing interests

Additional information

Extended data is available for this paper at https://doi.org/10.1038/s44161-023-00336-5.

Supplementary information The online version contains supplementary material available at https://doi.org/10.1038/s44161-023-00336-5.

Correspondence and requests for materials should be addressed to Chiara Giannarelli.

Peer review information *Nature Cardiovascular Research* thanks Peter Libby, Claudia Monaco and the other, anonymous, reviewer(s) for their contribution to the peer review of this work. Primary Handling Editor: Elvira Forte, in collaboration with the *Nature Cardiovascular Research* team.

Reprints and permissions information is available at www.nature.com/reprints.

Publisher's note Springer Nature remains neutral with regard to jurisdictional claims in published maps and institutional affiliations.

[1]Department of Medicine, Division of Cardiology, NYU Cardiovascular Research Center, New York University School of Medicine, New York, NY, USA. [2]Department of Microbiology, New York University School of Medicine, New York, NY, USA. [3]Precision Immunology Institute, Icahn School of Medicine at Mount Sinai, New York, NY, USA. [4]Department of Medicine, Cardiovascular Research Center, Icahn School of Medicine at Mount Sinai, New York, NY, USA. [5]Department of Microbiology, Icahn School of Medicine at Mount Sinai, New York, NY, USA. [6]Global Health and Emerging Pathogens Institute, Icahn School of Medicine at Mount Sinai, New York, NY, USA. [7]Department of Surgery, Vascular Division, Icahn School of Medicine at Mount Sinai, New York, NY, USA. [8]Department of Surgery, Vascular Division, New York University Langone Health, New York, NY, USA. [9]Department of Pathology, NYU Winthrop Hospital, Long Island School of Medicine, New York, NY, USA. [10]Department of Pathology, New York University School of Medicine, New York, NY, USA. ✉e-mail: chiara.giannarelli@nyulangone.org
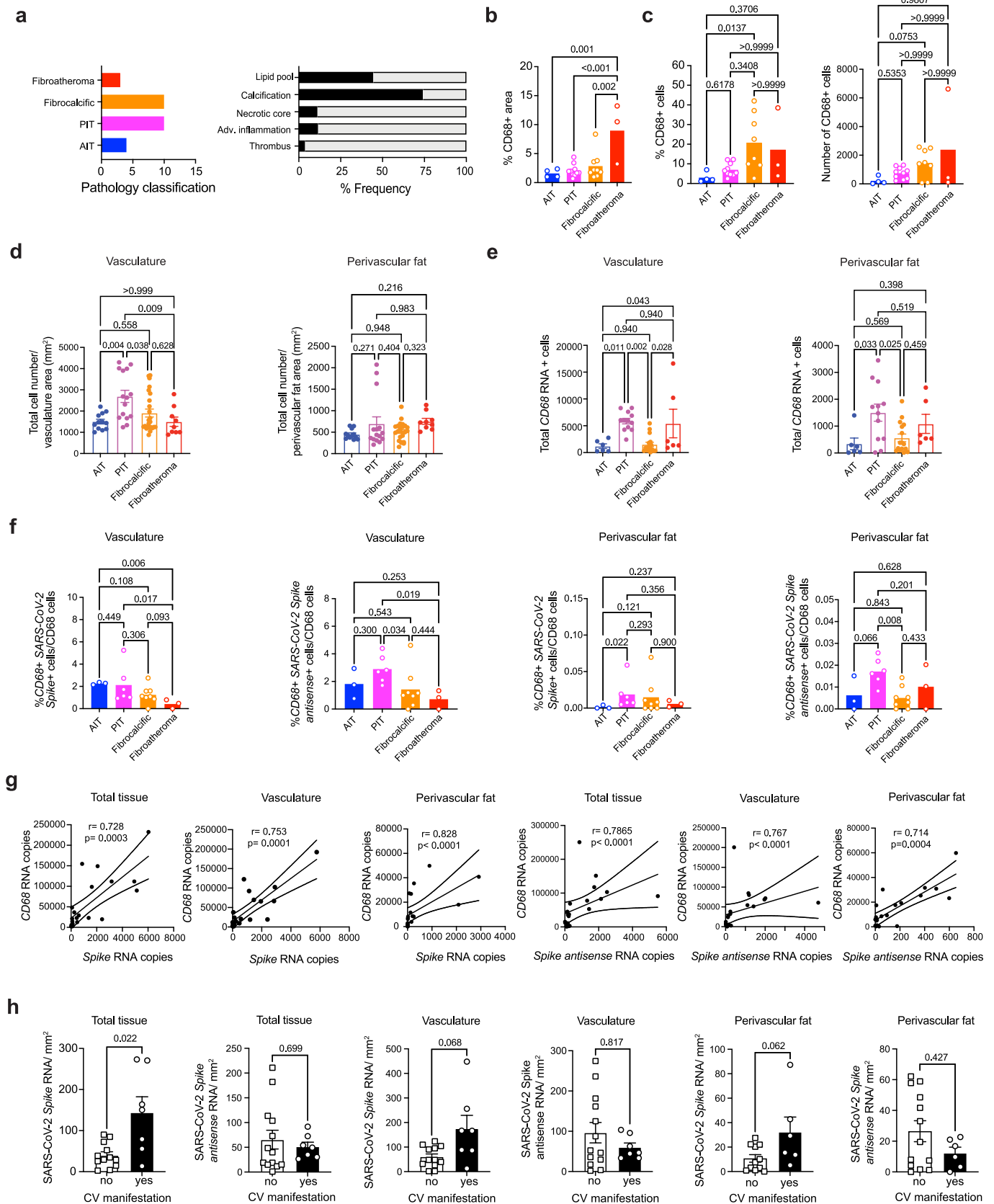
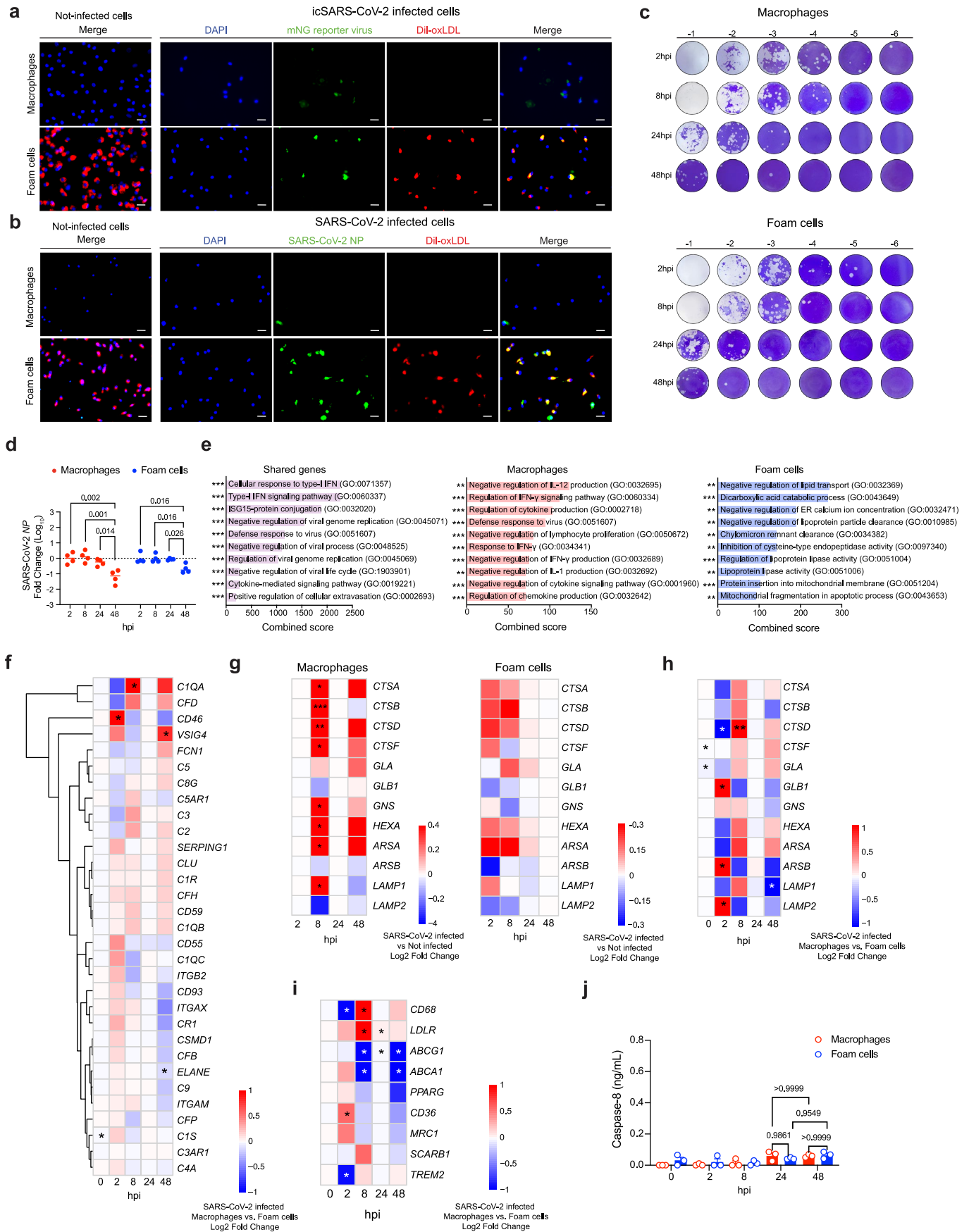**Extended Data Fig. 1 | See next page for caption.**

Extended Data Fig. 1 | Pathology assessment and RNA-FISH analysis of coronary arteries from deceased individuals with COVID-19. a) Bar plot (left) shows the number of adaptive intimal thickening (AIT; *blue*, $n = 4$), pathological intimal thickening (PIT; *magenta*, $n = 10$), fibrocalcific (*orange*, $n = 10$) and fibroatheroma (*red*, $n = 3$) specimens. Bar plot (right) shows the proportion of coronaries that presented pathological features of lipid pool, calcification, necrotic core, adventitial inflammation, and thrombus. **b)** Bar plot showing the percentage of CD68^{+} area. Non-parametric Kruskal-Wallis test with Dunn's test for multiple comparisons was performed. **c)** Bar plot showing the quantification of frequency and total count of CD68^{+} cells in AIT ($n = 4$), PIT ($n = 10$), fibrocalcific ($n = 8$) and fibroatheroma ($n = 3$). Data are presented as mean values ± s.e.m. Non-parametric Kruskal-Wallis test with Dunn's test for multiple comparisons was performed. **d)** Bar plots of total cell number normalized by the area (mm^2) of vasculature and perivascular fat. Each dot represents a tissue section from AIT ($n = 12$), PIT ($n = 15$), fibrocalcific ($n = 24$) and fibroatheroma ($n = 9$). Data are presented as mean values ± s.e.m. One-way ANOVA with post-hoc Tukey's test

for multiple comparisons was performed. **e)** Bar plots of total number of *CD68* RNA^{+} cells quantified in the arterial wall and perivascular fat. Dots represent individual tissue sections from AIT ($n = 6$), PIT ($n = 12$), fibrocalcific ($n = 16$) and fibroatheroma ($n = 6$). Data are presented as mean values ± s.e.m. One-way ANOVA followed by Holm-Šídák's test for multiple comparisons was performed. **f)** Bar plots of frequency of CD68^{+} SARS-CoV-2 Spike^{+} and CD68^{+} Spike antisense^{+} cells in AIT ($n = 3$), PIT ($n = 6$), fibrocalcific ($n = 8$) and fibroatheroma ($n = 3$) coronaries. Non-parametric Kruskal-Wallis test followed by uncorrected Dunn's test for multiple comparisons was performed. **g)** Scatter plot of Spearman's rank correlation (95% confidence interval) of total CD68 RNA copies with total SARS-CoV-2 spike and Spike antisense copies ($n = 20$). **h)** SARS-CoV-2 S and S antisense quantification in total tissue, vasculature, and perivascular fat from patients with ($n = 7$ samples) versus without CV manifestations ($n = 13$ samples). Data were normalized by tissue area (mm^2) and presented as mean values ± s.e.m. Rout method (Q = 1%) was used to remove outliers. Unpaired Mann-Whitney test was performed.
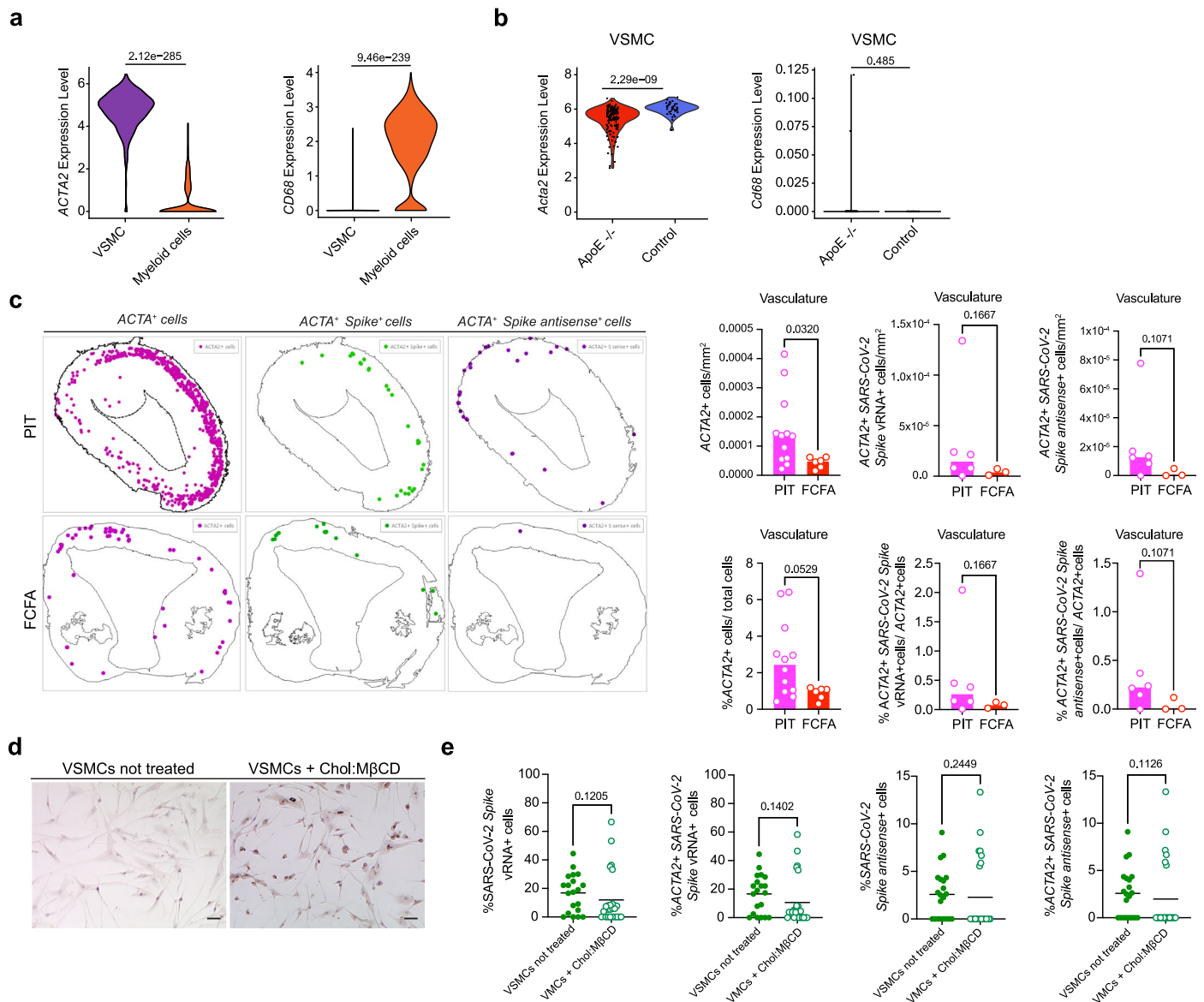
Extended Data Fig. 2 | Analysis of SARS-CoV-2 tropism for human vascular smooth muscle cells. a) Differential gene expression analysis of *ACTA2* and *CD68* in vascular smooth muscle cells (VSMCs) and myeloid cell clusters from seven atherosclerotic coronary samples. Wilcoxon Rank-Sum test was used to compare groups and adjusted p-values with Benjamini-Hochberg correction method are shown. **b)** Differential gene expression analysis of *Acta2* mRNA and *Cd68* mRNA in lineage-tagged (Tdt⁺) SMC-derived cells dissociated from the aortic arches of atherosclerotic single-color Tomato reporter (*Myh11-CreERT2, Rosa26tdTomato/tdTomato, ApoE⁻/⁻ mice*) mice fed high fat diet (HFD) for 18 weeks versus control mice. Wilcoxon Rank-Sum test was used to compare groups and adjusted p-values with BH correction method are shown. **c)** Representative images of spatial analysis of PIT coronary samples, and fibrocalcific and fibroatheroma (FCFA) samples showing the location of *ACTA2*⁺ cells, *ACTA2*⁺ SARS-CoV-2 Spike⁺ cells or *ACTA2*⁺ SARS-CoV-2 Spike antisense⁺ cells. Bar plots showing the number

and frequencies of *ACTA2*⁺ cells/mm², *ACTA2*⁺SARS-CoV-2 *Spike* vRNA⁺ and *ACTA2*⁺ SARS-CoV-2 S antisense⁺ cells normalized by tissue area (mm²) in intimal thickening (PIT; *n* = 6) versus fibrocalcific and fibroatheroma (*n* = 3) coronaries. Mann-Whitney test (two-tailed) was performed. **d)** Representative images of Oil Red-O staining of human VSMCs treated with 10 μg/mL of Cholesterol–methyl-β-cyclodextrin (Chol:MβCD) or vehicle overnight before infection and kept for 48 h. **e)** Bar plots showing the frequencies of SARS-CoV-2 *Spike* vRNA⁺, *ACTA2*⁺SARS-CoV-2 Spike vRNA⁺, SARS-CoV-2 S antisense⁺ and *ACTA2*⁺ SARS-CoV-2 *Spike* antisense⁺ cells in vehicle and Chol:MβCD conditions after infection with SARS-CoV-2 USA-WA1/2020 for 24 h. *n* = 20 of vehicle and *n* = 25 Chol:MβCD treated VSMCs in *Spike* vRNA quantification experiment, *n* = 21 of vehicle and *n* = 24 Chol:MβCD treated VSMCs in *Spike* antisense quantification experiment. Mann-Whitney test (two-tailed) was used.

Extended Data Fig. 3 | See next page for caption.

Extended Data Fig. 3 | SARS-CoV-2 in-vitro infection of human primary macrophages and foam cells. a) Representative images of not-infected and infected macrophages and foam cells cultured with mNG reporter virus (MOI 0.1) at 24 hpi. Scale bar, 20 μm. **b)** Representative images of not-infected and SARS-CoV-2 infected macrophages and foam cells at 24 hours post-infection (hpi). Scale bar, 20 μm. **c)** Representative images of plaque assay in VERO E6-TMPRSS2-T2A-ACE2 cells of culture supernatants of macrophages and foam cells cultured with SARS-CoV-2 USA- WA1/2020 at 2 hpi, 8 hpi, 24 hpi, and 48 hpi. Serial dilutions are represented from left to right (-1 to -6). **d)** Bar plot showing the $\log_{10}$ FC of SARS-CoV-2 NP RNA levels normalized by 2 hpi samples ($n = 4$ biological replicates) in infected macrophages and foam cells. **e)** Bar plots showing the combined score of Gene Ontology (GO) Biological Process 2021 enrichment analysis of upregulated genes in infected macrophages, foam cells and or both vs. non-infected counterparts. $P < 0.05$. *, $P < 0.05$; **, $P < 0.01$; ***, $P < 0.001$. **f)** Heat map of $\log_2$ FC in complement genes between SARS-CoV-2 infected macrophages ($n = 3$) and SARS-CoV-2 infected foam cells ($n = 3$) at 0 hpi, 2 hpi, 8 hpi, 24 hpi and 48 hpi. Adjusted P-values < 0.05 (FDR = 10%) were considered significant. **g)** Heat map of $\log_2$ fold changes in lysosomal genes in SARS-CoV-2 infected cells vs. not infected cells at 2 hpi, 8 hpi, 24 hpi and 48 hpi. **h)** Heat map of $\log_2$ fold changes in lysosomal genes in SARS-CoV-2 infected macrophages vs. foam cells at 2 hpi, 8 hpi, 24 hpi and 48 hpi. P-values < 0.05 were considered significant. $P < 0.05$. *, $P < 0.05$; **, $P < 0.01$; ***, $P < 0.001$. **i)** Heat map of $\log_2$ FC in lipid metabolism genes in SARS-CoV-2 infected macrophages ($n = 3$) vs. foam cells ($n = 3$) at 2 hpi, 8 hpi, 24 hpi and 48 hpi. Adjusted P-values < 0.05 (FDR = 0.1) were considered significant. $P < 0.05$. *, $P < 0.05$; **, $P < 0.01$; ***, $P < 0.001$. **j)** Quantification of Caspase-8 concentration in culture supernatants of not infected or SARS-CoV-2 infected macrophages and foam cells. One-way ANOVA with post-hoc Tukey's test were performed.
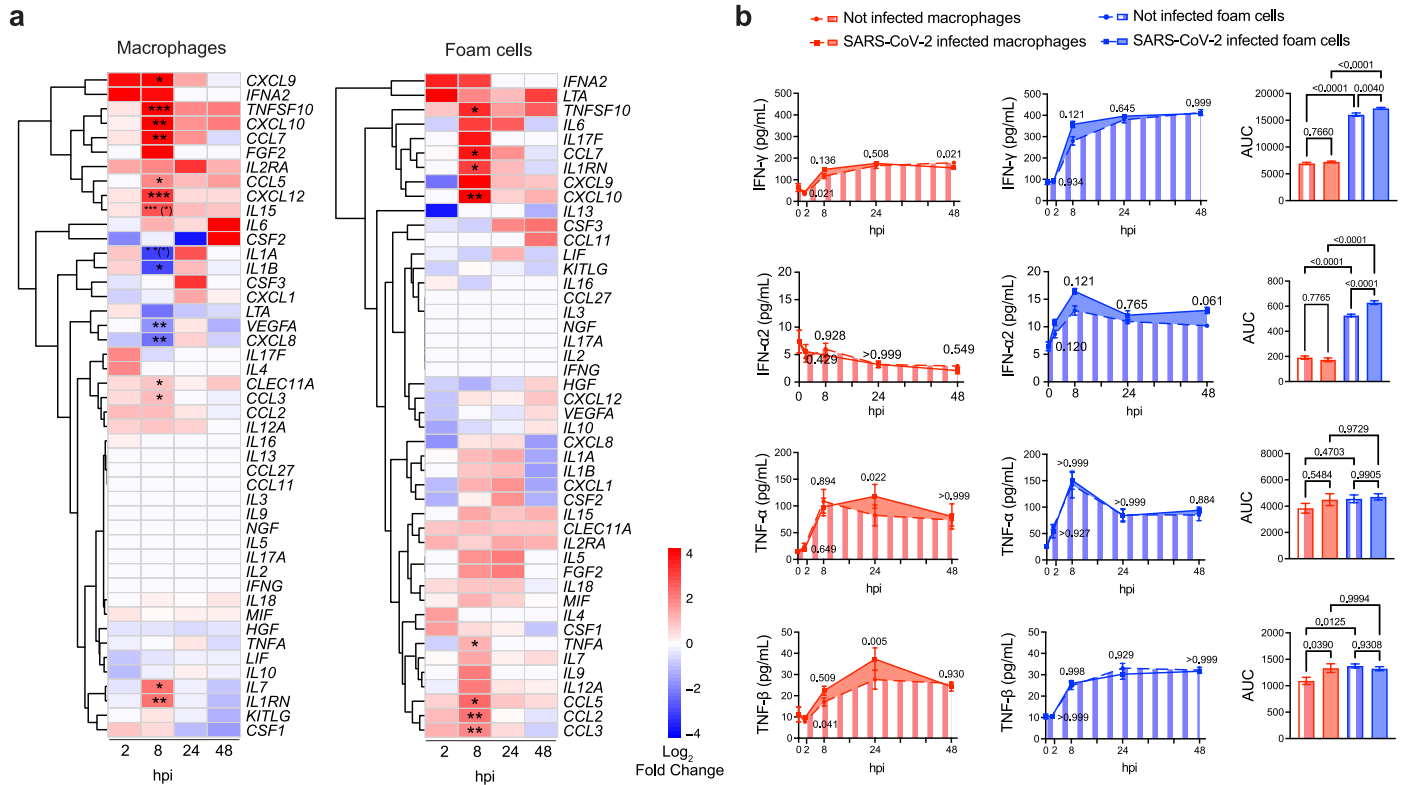
Extended Data Fig. 4 | Dynamics of cytokine response in macrophages and foam cells after SARS-CoV-2 infection. a) Heat maps of log$_2$ FC of selected differentially expressed cytokine and chemokine genes in SARS-CoV-2 infected macrophages (*left*, n = 3) and foam cells (*right*, n = 3) versus. non-infected counterparts at different hpi. *P*-values were adjusted using Benjamini-Hochberg correction (FDR = 10%). Adjusted *P*-values < 0.05 were considered significant. Asterisk indicates an adjusted *P*-value < 0.05 for the comparison of infected vs not infected at each timepoint. Asterisk in parentheses indicates an adjusted *P* value < 0.05 for the interaction term of the model. *, *P* < 0.05; **, *P* < 0.01; ***, *P* < 0.001. **b)** Kinetic plots showing the area under the curve (AUC) of cytokines and chemokines in the supernatant of SARS-CoV-2 infected and non-infected macrophages and foam cells (*n* = 4 biological replicates, technical duplicates). For AUC comparisons, one-way ANOVA with Tukey's test for multiple comparisons was used. Bar plots represent Mean ± s.e.m. One-way ANOVA followed by Šídák's test for multiple comparisons was performed.
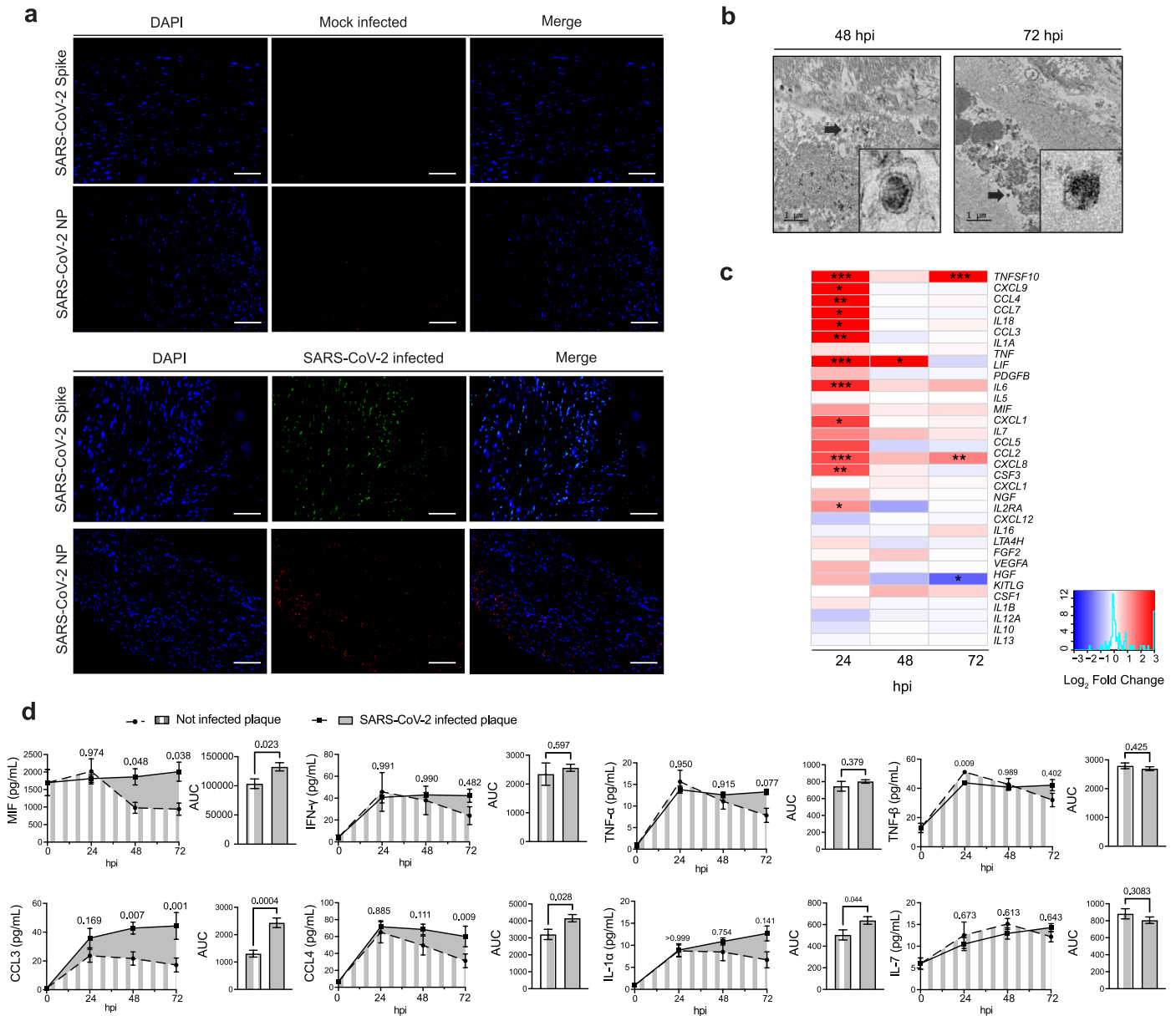
Extended Data Fig. 5 | Ex-vivo SARS-CoV-2 infection of human carotid vascular explants. a) Representative images of human atherosclerotic plaque tissues infected ex vivo with SARS-CoV-2 USA-WA1/2020 (10⁵ PFU) versus mock infected control shows the expression of spike protein and nucleoprotein (NP). Scale bar, 100 μm. **b)** Electron microscopy of human atherosclerotic carotid plaque tissue infected ex vivo with the SARS-CoV-2. Scale bar, 1 μm. Black arrows indicate coronavirus-like particles. **c)** Heat map of selected cytokine and chemokine genes showing the $\log_2$ FC in SARS-CoV-2 infected carotid vascular explants versus not-infected tissues at different times post-infection. Wald test from DESeq2 package was used to test for significance. P values were adjusted using Benjamini-Hochberg correction (FDR = 10%) and denoted as an asterisk *, $P < 0.05$; **, $P < 0.01$; ***, $P < 0.001$. **d)** Kinetic plots showing the AUC of selected cytokines and chemokines secreted by non-infected or SARS-CoV-2 infected carotid vascular explants (n = 3 donors, technical duplicates) at different time post-infection. One-way ANOVA with Šídák's test for multiple comparisons was performed. Bar plots represent mean ± s.e.m. Unpaired t-test (two-tailed) was performed and $P < 0.05$ was considered significant.
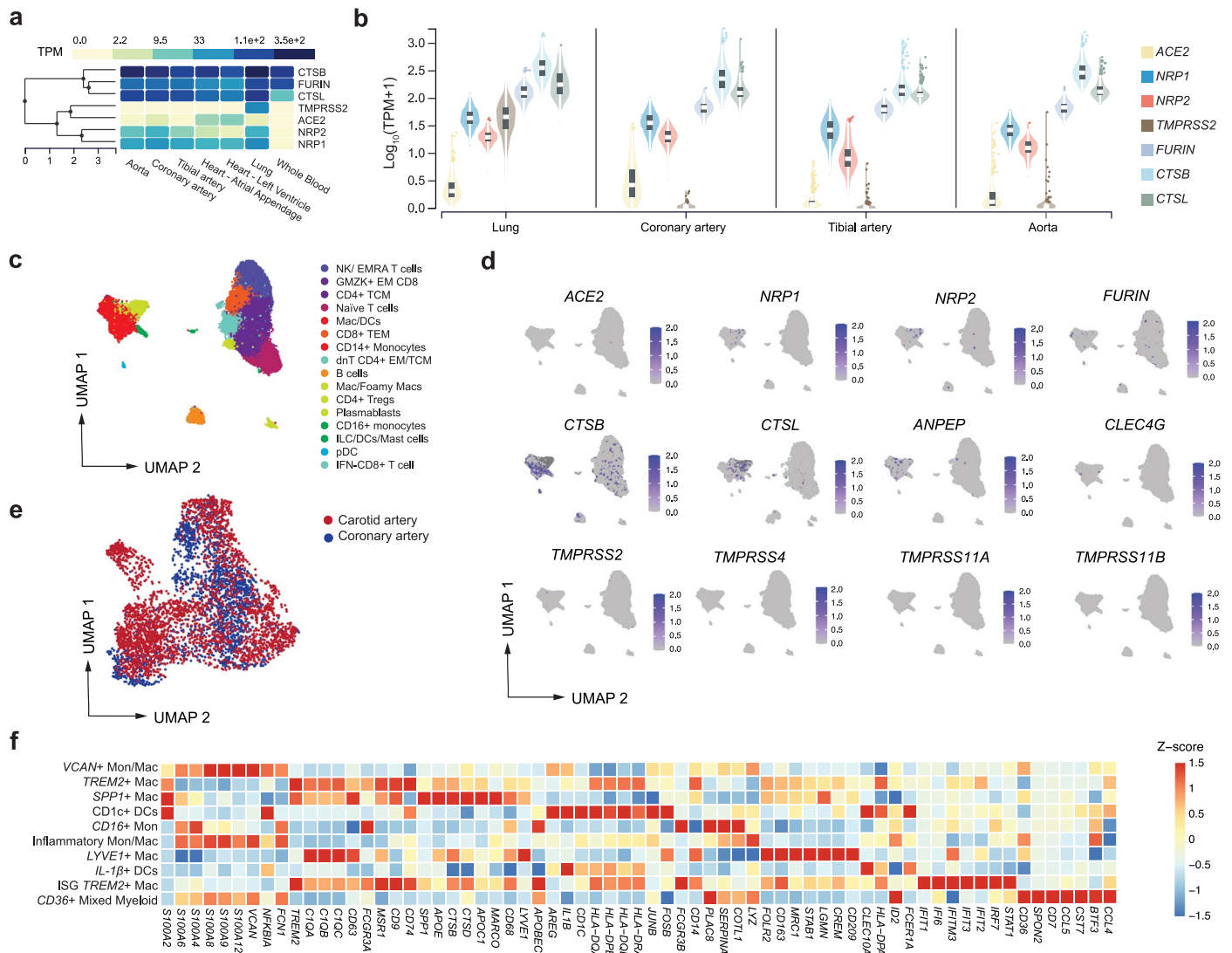
Extended Data Fig. 6 | Single cell RNA sequencing analysis of SARS-CoV-2 entry factors in vascular myeloid subclusters. a) Heat map shows transcripts expression (median *TPM*, transcripts per million) of SARS-CoV-2 entry factors identified in lung, whole blood, heart (left ventricle and atrial appendage), aorta, and tibial and coronary arteries. **b)** Violin plots showing the $\log_{10}$ TMP + 1 of tissue level expression of SARS-CoV-2 entry factors in lung, aorta, tibial and coronary artery identified. Data are presented as median ±IQR (25%-75% quartiles) in the box plot, violin plot defines density of data in whole range. **c)** UMAP embedding of integrated total immune cells from carotid (n = 10) and coronary (n = 7) tissues. **d)** Gene expression of SARS-CoV-2 viral entry factors and related genes projected onto the UMAP of total immune cells. **e)** UMAP representation of myeloid cell clusters colored by tissue origin. Dots represent individual cells belonging to carotid (*red*) or coronary artery (*blue*). **f)** Heatmap displaying selected *z*-score scaled genes (*columns*) across myeloid cell subclusters (*rows*) from human coronary and carotid samples. Canonical genes were used for myeloid subclusters annotations.
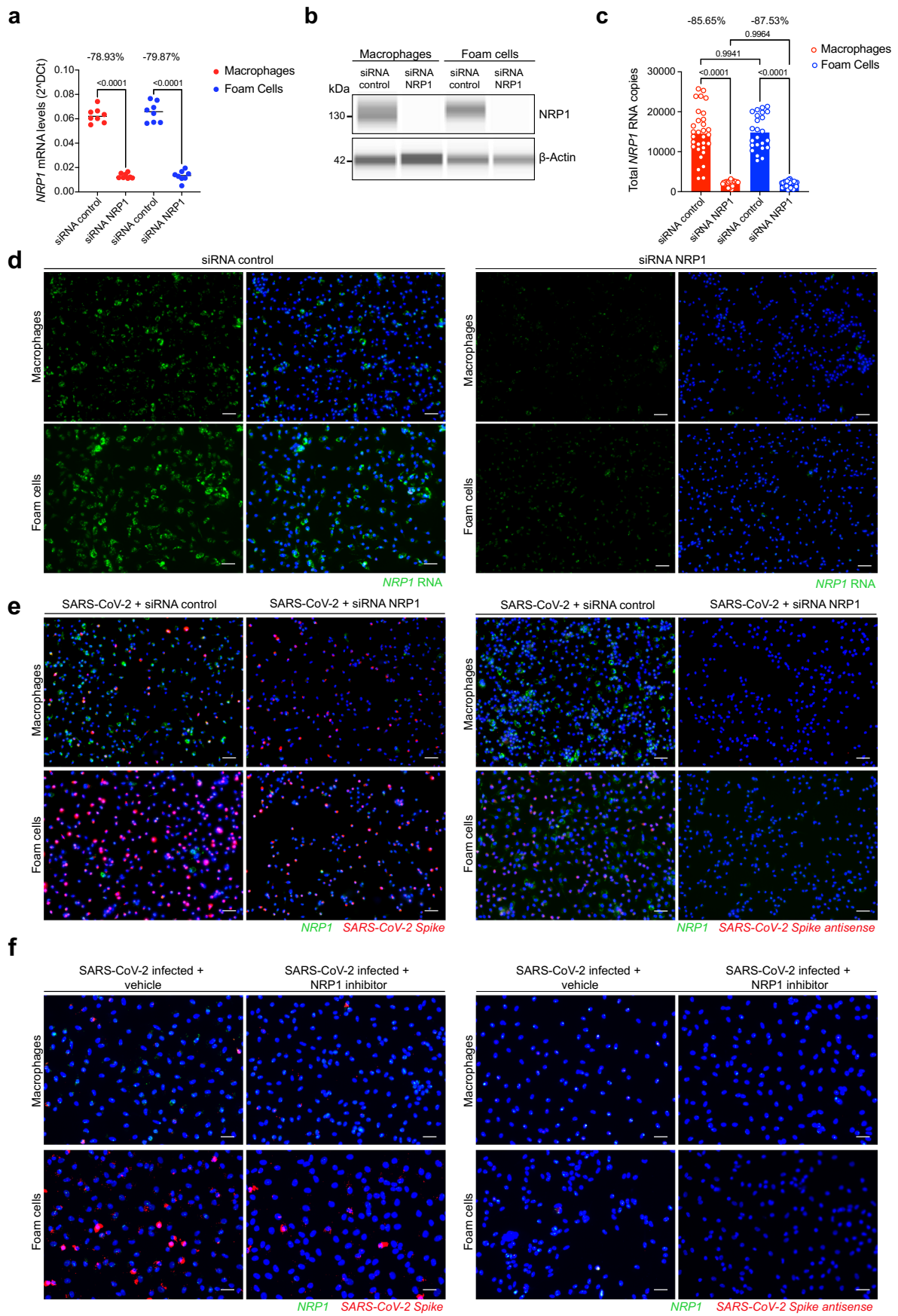
Extended Data Fig. 7 | See next page for caption.

Extended Data Fig. 7 | Abrogation of SARS-CoV-2 interaction with host by NRP-1 small molecule inhibitor and silencing RNA. a) Dot plot showing the relative expression levels of *NRP1* RNA normalized by *GAPDH* RNA expression in macrophages and foam cells. Average percentage of *NRP1* silencing efficacy were calculated and depicted at the top (*n* = 4 biological replicates measured by technical duplicate per cell type, condition). **b)** Representative image of capillary western blot (Wes) was performed to evaluate the protein expression levels of NRP1 after siRNA *NRP1* or siRNA control treatment. Target protein NRP1 (130-140 kD) and β-actin loading control blots (42 kD) are shown. **c)** Total *NRP1* RNA copies were quantified in not-infected macrophages and foam cells treated with either siRNA control or siRNA NRP1 (*n* = 31 images of macrophages siRNA

control; *n* = 26 macrophages siRNA NRP1, *n* = 24 foam cells siRNA control, *n* = 25 foam cells siRNA NRP1) at 24 hpi. **d)** Representative images and quantification of RNA-FISH showing *NRP1* RNA in not-infected macrophages and foam cells. **e)** Representative images of RNA-FISH showing SARS-CoV-2 spike vRNA and *NRP1* RNA (left), SARS-CoV-2 spike antisense vRNA and *NRP1* RNA (*right*) in infected macrophages and foam cells treated with non-targeting siRNA control or siRNA NRP1 at 24 hpi. **f)** Representative images of RNA-FISH showing SARS-CoV-2 S vRNA and *NRP1* RNA (left), SARS-CoV-2 S antisense RNA and *NRP1* RNA (*right*) in infected macrophages and foam cells with and without NRP1-blocking (EG00229 trifluoroacetate) at 24 hpi.
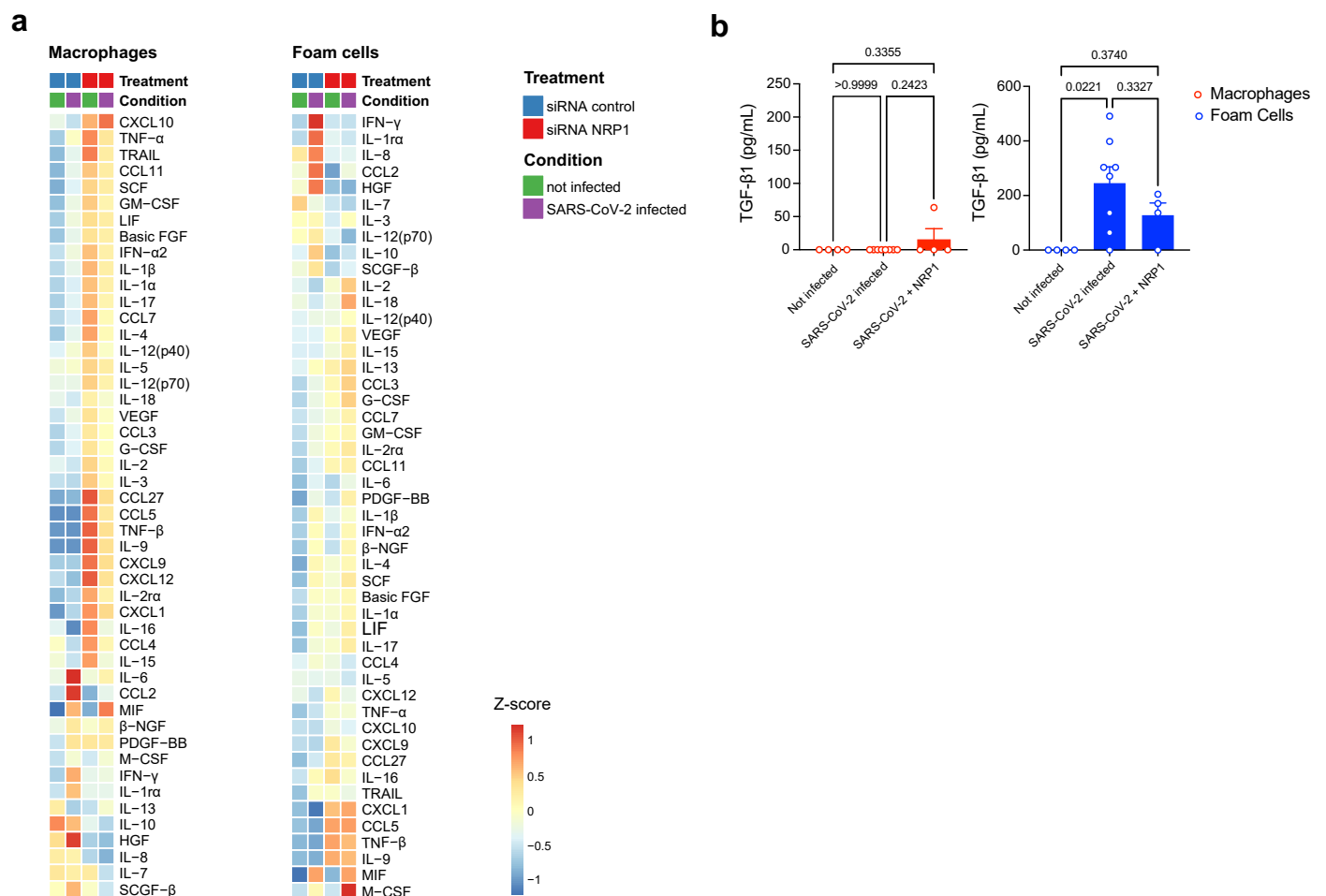
Extended Data Fig. 8 | Dynamics of cytokine response in NRP1- blocking/silencing treated macrophages and foam cells. a) Heat map of standardized z-scored gene expression of cytokines and chemokines in not-infected, SARS-CoV-2 infected macrophages and foam cells treated with non-targeting siRNA control or siRNA NRP1 at 24 hpi. **b)** Quantification of TGF-β1 concentration (pg mL⁻¹) in culture supernatants of not infected (n = 4) or SARS-CoV-2 infected macrophages and foam cells with (n = 4) or without (n = 8) NRP1-blocking treatment (EG00229 trifluoroacetate) at 24 hpi. Data are presented as mean values ±s.e.m. One-way ANOVA with post-hoc Tukey's test for multiple comparisons was performed.

Corresponding author(s):   Dr. Chiara Giannarelli

Last updated by author(s):   Aug 18, 2023

Reporting Summary

Nature Portfolio wishes to improve the reproducibility of the work that we publish. This form provides structure for consistency and transparency in reporting. For further information on Nature Portfolio policies, see our Editorial Policies and the Editorial Policy Checklist.

Statistics

For all statistical analyses, confirm that the following items are present in the figure legend, table legend, main text, or Methods section.

n/a	Confirmed	
☐	☒	The exact sample size (*n*) for each experimental group/condition, given as a discrete number and unit of measurement
☐	☒	A statement on whether measurements were taken from distinct samples or whether the same sample was measured repeatedly
☐	☒	The statistical test(s) used AND whether they are one- or two-sided *Only common tests should be described solely by name; describe more complex techniques in the Methods section.*
☐	☒	A description of all covariates tested
☒	☐	A description of any assumptions or corrections, such as tests of normality and adjustment for multiple comparisons
☐	☒	A full description of the statistical parameters including central tendency (e.g. means) or other basic estimates (e.g. regression coefficient) AND variation (e.g. standard deviation) or associated estimates of uncertainty (e.g. confidence intervals)
☐	☒	For null hypothesis testing, the test statistic (e.g. *F*, *t*, *r*) with confidence intervals, effect sizes, degrees of freedom and *P* value noted *Give P values as exact values whenever suitable.*
☒	☐	For Bayesian analysis, information on the choice of priors and Markov chain Monte Carlo settings
☐	☒	For hierarchical and complex designs, identification of the appropriate level for tests and full reporting of outcomes
☐	☒	Estimates of effect sizes (e.g. Cohen's *d*, Pearson's *r*), indicating how they were calculated

Our web collection on statistics for biologists contains articles on many of the points above.

Software and code

Policy information about availability of computer code

Data collection	No software was used to collect data
Data analysis	Statistical analyisis was performed in GraphPad Prism 9, Version 9.5.0 (525). For pathology and spatial analysis the following softwares were used: HALO image Analysis platform and AI version 3.5.3577 and version 3.6.4134 (Indica Labs, Inc.). Design and Analysis Software Version 2.6 (Applied Biosystems) were used for RT-PCR analysis. Single-cell RNAseq, bulk RNAseq and Luminex were analyzed with Seurat package (v4.0.3), CellRanger (10X Genomics v3.1.0), FastQC2 (v.0.11.7), STAR (v.2.6.1d), R (v.4.0.3), R package DESeq2 (v1.30.1), pheatmap package (v1.0.12). Pathway analysis was performed with Enrichr v3 hosted at https://maayanlab.cloud/Enrichr/. Code used for data analysis is available on GitHub at https://github.com/giannarelli-lab/SARS-CoV-2-infection-triggers-pro-atherogenic-inflammatory-responses-in-human-coronary-vessels.

For manuscripts utilizing custom algorithms or software that are central to the research but not yet described in published literature, software must be made available to editors and reviewers. We strongly encourage code deposition in a community repository (e.g. GitHub). See the Nature Portfolio guidelines for submitting code & software for further information.

Data

Policy information about availability of data

All manuscripts must include a data availability statement. This statement should provide the following information, where applicable:
- Accession codes, unique identifiers, or web links for publicly available datasets
- A description of any restrictions on data availability
- For clinical datasets or third party data, please ensure that the statement adheres to our policy

Single cell RNA sequencing data from the 6 human carotid arteries were previously published and are available in Gene Expression Omnibus (GEO) NCBI (GSE224273). Four additional carotid plaques were processed to obtain sc-RNAseq data deposited in GEO NCBI (GSE235437). scRNA-seq data coronary lesions were obtained from GEO NCBI (GSE131780). Bulk RNA sequencing data from macrophages and foam cell experiments and the plaque tissues infected with SARS-CoV-2 are deposited in GEO repository (GEO:GSE235437). All other data supporting the findings in this study are included in the main article and associated files. Source data files are available on GitHub at https://github.com/giannarelli-lab/SARS-CoV-2-infection-triggers-pro-atherogenic-inflammatory-responses-in-human-coronary-vessels.
GTEx data used in Extended Data Figure 6 is available at the GTEx Portal (https://www.gtexportal.org/home) For this manuscript the data used was version V8, dbGaP Accession phs000424.v8.p2.
Murine single-cell RNA-seq data used in Extended Figure 2 from from Wang et al. (2020) was extracted from BioProject Accession: PRJNA626450 (https://www.ncbi.nlm.nih.gov/bioproject/626450).
Human (Homo sapiens) genome assembly GRCh38 (hg38) was obtained from Genome Reference Consortium [GCA_000001405.15 GCF_000001405.26])
SARS-CoV-2 Washington isolate (WA1/2020) genome (GeneBank: MN985325.1) was obtained from the NIH repository https://www.ncbi.nlm.nih.gov/nuccore/MN985325

Human research participants

Policy information about studies involving human research participants and Sex and Gender in Research.

Reporting on sex and gender	We refer to biological sex in the manuscript, although we did not investigate sex differences in the current manuscript. We did not actively select the sex or gender of the enrolled patients.
Population characteristics	Supplementary Table S1 and S2 describe demographics and clinical history of cohort of COVID-19 patients. Patient cohort consisted in 8 patients (75% male), ethnicity 62.5% non-hispanic or latino, 37.5% unknown or not reported, race 37.5% black or african american, 37.5% unknown or not reported, 12.5% white and 12.5% more than one race. Supplementary Table S4 describes the clinical history and demographics of patients enrolled in the study for single cell RNAseq analysis. Patient cohort in 10 patients (90% male), ethnicity 90% non-hispanic or latino, 10% not reported, race 50% white, 20 % african american, 20% asian and 10% more than one race or not reported, median age 68.5 years old (range 62-93).
Recruitment	All adult patients are recruited that meet the study by the responsible research coordinators priot to carotid endarterectomy surgery. Patients included in the study get a study ID and remain anonymous for the rest of the study. The recruitment process for participants in this study is designed to minimize bias and ensure a comprehensive representation of eligible individuals. All patients who meet the predetermined enrolling criteria and have provided informed consent are enrolled, without any form of bias.
Ethics oversight	Post-mortem coronary artery specimens from 8 patients diagnosed with COVID-19 were obtained from the NYU Langone Health and NYU School of Medicine's Center for Biospecimen Research and Development (CBRD), with approval by the Institutional Review Board of NYU Langone Health for (IRB i21-01587). Patients undergoing carotid endarterectomy (CEA) were enrolled in the ATHERO-IN study, an observational clinical study approved by the Institutional Review Boards of the Icahn School of Medicine at Mount Sinai (IRB 11–01427) and the NYULH (IRB i21-00429).

Note that full information on the approval of the study protocol must also be provided in the manuscript.

Field-specific reporting

Please select the one below that is the best fit for your research. If you are not sure, read the appropriate sections before making your selection.

☒ Life sciences   ☐ Behavioural & social sciences   ☐ Ecological, evolutionary & environmental sciences

For a reference copy of the document with all sections, see nature.com/documents/nr-reporting-summary-flat.pdf

Life sciences study design

All studies must disclose on these points even when the disclosure is negative.

Sample size	No a-priori sample size calculation was performed for the study. We have included all possible samples that were available at the time of

Sample size	experiments.
Data exclusions	No samples were excluded from the analysis
Replication	Experiments were replicated at least once for the immunohistochemical, immunofluorescence and RNAscope and in-vitro studies involving NRP1 inhibitor and NRP1 siRNA analysis. For bulk-RNA and Luminex, a minimum of two/three samples per group or condition were used. All attempts at experimental replication were successful.
Randomization	Randomization was not employed in this study due to the unique characteristics of our target population and the specific nature of the interventions being investigated. The nature of our study design involved a specific target population with unique characteristics that could not be easily randomized. For COVID-19 patients' post-mortem samples, samples were obtained from NYU Center for Biospecimen Research and Development (CBRD) based on availability. For CEA studies we did not actively randomize our patients, as the samples were processed from prospectively enrolled patients.
Blinding	For the studies using human specimens, we used unbiased computational approaches to analyze the data. Bioinformatitians and investigators are blinded to the study conditions and experimental designs for the analysis.

Reporting for specific materials, systems and methods

We require information from authors about some types of materials, experimental systems and methods used in many studies. Here, indicate whether each material, system or method listed is relevant to your study. If you are not sure if a list item applies to your research, read the appropriate section before selecting a response.

Materials & experimental systems

n/a	Involved in the study
☐	☒ Antibodies
☐	☒ Eukaryotic cell lines
☒	☐ Palaeontology and archaeology
☒	☐ Animals and other organisms
☒	☐ Clinical data
☒	☐ Dual use research of concern

Methods

n/a	Involved in the study
☒	☐ ChIP-seq
☒	☐ Flow cytometry
☒	☐ MRI-based neuroimaging

Antibodies

Antibodies used	The following antibodies were used: Mouse anti-human CD68 (KP1) 760-2037 Ventana Medical Systems (pre-diluted. Cat# 760-2931, Lot#'s H354244, H15799, RRID AB_2335972); human Neuropilin-1 Antibody Cat. #AF3870 R&D Systems (1:100); CD68 Monoclonal Antibody (KP1), eBioscience Cat. #14-0688-82 Invitrogen (1:100); Goat anti-Mouse IgG (H+L) Highly Cross-Adsorbed Secondary Antibody, Alexa Fluor 594 Cat. #A11032 Invitrogen (2:400); Goat anti-Rabbit IgG (H+L) Cross-Adsorbed Secondary Antibody, Alexa Fluor Cat. #488 A-11008 Invitrogen (1:400); Goat anti-Mouse IgG (H+L) Cross-Adsorbed Secondary Antibody, Alexa Fluor 488 Cat. #A-11001 Invitrogen (1:400); anti-SARS-CoV-2 Nucleocapsid Antibody clone 1C7 Cat. # 10-605 ProScience (1:100); goat anti-mouse Alexa Fluor 488 A11001 Invitrogen (1:400); anti-NRP1 rabbit monoclonal antibody 3725 Cell Signaling (1:50); anti-β-actin mouse monoclonal antibody A2228 Sigma Aldrich (1:500); anti-rabbit HRP conjugated antibody Cat. #042-206 Protein Simple; anti-mouse HRP conjugated antibody Cat. #031-108 Protein Simple.
Validation	All antibodies were validated for the applications in this manuscript by the correspondent manufacturer and the information is located in their website. Our usage was described in the Methods section of the manuscript.

Eukaryotic cell lines

Policy information about cell lines and Sex and Gender in Research

Cell line source(s)	Cells used in this study are the following: Vero E6 (American Type Culture Collection; Cercopithecus aethiops Kidney Epithelial Cells) obtained from ATC, Cat #CRL-1586. Vero E6 Expressing Transmembrane Protease, Serine 2 and Human Angiotensin-Converting Enzyme 2 (Vero E6-TMPRSS2-T2A-ACE2) obtained from Biodefense and Emerging Infections Research Resources Repository (BEI Resources), Cat. #NR-54970 Human Peripheral Blood Monocytes obtained from StemCell Technologies , Cat. #200-0167 Human Aortic Smooth Muscle Cells (HAoSMC) obtained from PromoCell, Cat. #C-12533
Authentication	All cell lines were recently purchased from vendors. We did not do in-house authentication of cell lines.
Mycoplasma contamination	Cell lines were confirmed to be negative for Mycoplasma contamination with MycoAlert Detection kit (Lonza).

Commonly misidentified lines
(See ICLAC register)

No commonly misidentifed cell lines were used in this study according to ICLAC register of misidentified cell lines.